Improving Performance of a Multiplexed Dark Matter Detector via Infrared Isolation

A Thesis Presented in Partial Fulfillment of

the Honors Bachelor's Degree

Gabriel Spahn

Abstract

Microwave Kinetic Inductance Detectors (MKIDs) are superconducting microresonators that are most commonly used for microwave detection in astronomy. They have potential for use as phonon detectors in cryogenic dark matter searches, but their implementation faces a number of technical challenges. Among these issues is the potential for higher-temperature infrared photons to reach the superconducting substrate and consequently degrade the quality factor of the MKID's resonance. This thesis details the design and construction of epoxy-based filters meant to mitigate this effect, and finds that their installation in the readout system for an Al MKID increased its quality factor by an average of 12% across a range of operating temperatures and powers.

UNIVERSITY OF MINNESOTA

School of Physics and Astronomy

Under the supervision of Drs. Vuk Mandic and Noah Kurinsky

University of Minnesota Twin Cities

April 2021

Acknowledgments

Many thanks go to all those who helped me over the course of researching and writing this thesis; it wouldn't have been possible without them. Special thanks go to Noah Kurinsky for his constant advising with everything from the first experimenting to the final write-up, Vuk Mandic for his advising and support of the initial UROP for this project, Matt Hollister for his help with filter design, Dan Bauer for somehow getting me lab space during a global pandemic, Akash Dixit for his aid in constructing the HFSS simulations, Ziqing Hong for his help and expertise constructing epoxy filters, Osmond Wen for offering his experience with MKID readout and data analysis, and Priscilla Cushman for acting as the independent reader.

Contents

1 Introduction

The existence of dark matter, confirmed by a wide array of cosmological and astronomical experiments, has been a largely settled debate for decades. In that time, experiments have probed large swathes of parameter space to ascertain its exact nature, but none have returned a positive result. In the light-mass fermionic regime, solid-state cryogenic experiments such as SuperCDMS, EDELWEISS and CRESST have probed down past 0.2GeV using a variety of crystal calorimeters [1]. Looking ahead to the realm of sub-GeV-mass dark matter, this detector design encounters difficulties with scalability. Higher sensitivity requires larger amounts of instrumented surface area, but each individual detector requires its own dedicated readout chain; using larger crystals for each detector increases both fabrication costs and the complexity of electron transport dynamics [2].In light of these challenges, there has been increased investigation into the use of other, more scalable cryogenic detector designs.

The Microwave Kinetic Inductance Detector (MKID) design has potential for this application. It consists of a thin film of superconducting material patterned onto a semiconductor substrate then capacitively coupled to a feedline. When an AC field is applied to the MKID via the feedline, the inertia of the superconducting charge carriers, or Cooper pairs, causes their motion to lag behind that of the driving electric field. This effect lends the film a so-called "kinetic inductance." This inductance, combined with the capacitive coupling, results in a resonant LC circuit with high Q factor. The fundamental frequency and quality factor of the resonance both depend on the ratio of superconducting Cooper pairs to quasiparticles in the substrate. That ratio is theoretically sensitive to the presence of dark matter; any particle incident on the substrate would generate phonons that could break Cooper pairs into quasiparticles, changing the resonating behavior of the device in quantifiable ways (Figure 1).

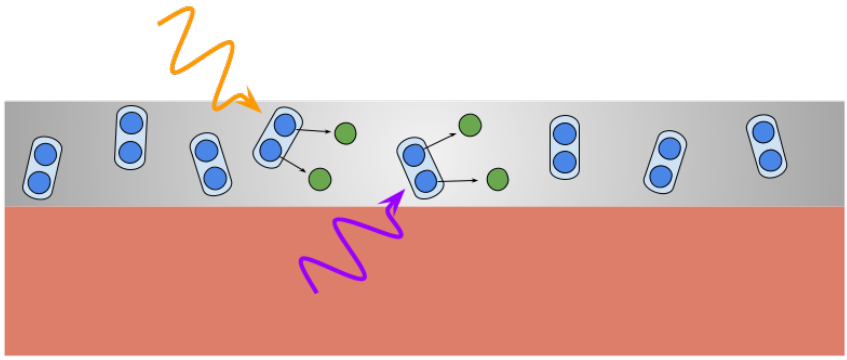

Figure 1: A superconducting thin film (silver) sits on top of a semiconductor substrate (red). A photon incident from above (orange) breaks a Cooper pair of two bound electrons (blue) into two unbound quasiparticles (green). A phonon incident on the film from underneath (purple) does the same. It is assumed that both photon and phonon have energy at least equal to twice the superconducting gap energy.

One obstacle to using MKIDs in this manner is the incidence of background IR photons onto the superconducting substrate. These photons are typically generated by warmer temperature stages of the cryogenic system housing the MKIDs, and travel down to the detector level by hijacking data and power lines. Those with high enough energy then break apart a Cooper pair into quasiparticles, reducing the resonator's quality factor and consequently its sensitivity. The best way to prevent this phenomenon is to place filters on all conducting lines that run from higher temperatures down to the detectors; however, no IR filters of small enough size for this application are currently commercially available.

This thesis describes the design and assembly of epoxy-based inline IR filters. Then, paired with a discussion of MKID dynamics, it examines their effect on the sensitivity of an MKID-based dark matter detector and overall success in blocking IR noise. While these filters were designed with an MKID application in mind, they are potentially useful to any experiment involving high-sensitivity superconducting elements, including the input stage of quantum computers utilizing superconducting qubits.

2 Microwave Kinetic Inductance Detectors

Microwave Kinetic Inductance Detectors (MKIDs) are thin-film superconducting resonators that have found previous application in far-infrared astronomy. At the simplest design level, they consist of a superconducting film patterned onto a substrate in order to form inductive and capacitive elements. The MKID tested in this investigation is made up of an interdigitated niobium capacitor and meandered aluminum inductor (Figure 2a) fabricated onto a silicon crystal. The kinetic inductance that gives MKIDs their name comes from the inertia of the Cooper pairs that carry superconducting current inside the film; in the presence of an alternating electric field, the mass of these pairs causes their motion to lag behind that of the field. This kinetic inductance combines with the geometric inductance, capacitance, and film surface resistance to form an RLC circuit with resonating behavior. Both the characteristic frequency and sharpness of that resonance are derived from the system's complex inductance and resistance.

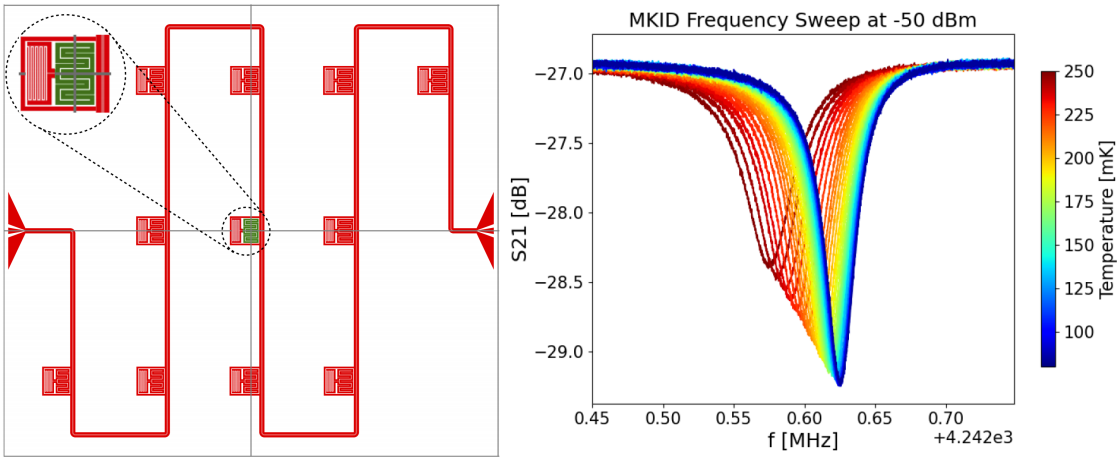

Figure 2: a (left): Layout and design of MKIDs used in this investigation; green denotes aluminum, red denotes niobium. The feedline and all capacitors are Nb in order to be insensitive to phonons (due to Nb's higher gap energy). The MKID with the aluminum inductor (inset) is the only one used for phonon detection; all others are used only for calibration. Besides this, each device uses the same design (apart from varying ω_0). The size of each inductor is approximately 1 mm. b (right): S21 parameter frequency sweep of the measurement feedline coupled to the Al MKID in a).

These properties of an MKID are observed via stimulation by a feedline that couples with its capacitive element, as shown in the inset of Figure 2a. If the feedline signal's frequency is near the resonance of the MKID, a large current will be excited in the detector; by energy conservation, there must be a corresponding drop in the signal strength inside the feedline. Thus, the ratio of the feedline's output signal strength to the strength of the initial excitation will depend on the distance between the excitation signal frequency and the MKID resonance frequency. Viewing the system as a two-port network, with the feedline input as port 1 and the feedline output as port 2, this ratio is equivalent to the $S21$ transmission parameter; measuring its value

over a range of frequencies will produce the "notch" shape visible in Figure 2b. This plot shows how the shape and location of the notch changes as a function of temperature; because an increase in temperature breaks Cooper pairs in a roughly similar way to a particle incident on the detector, the behavior in Figure 2b also shows how the MKID functions as a calorimeter.

Breaking a number of Cooper pairs into quasiparticles impacts multiple characteristics of the detector. First, the surface resistance of the film increases, because there are more electrons in a normal conducting state. This increases the damping of the resonant behavior, leading to a smaller resonance peak. This is visible in Figure 2b, with both the depth and sharpness of the notches decreasing at higher temperatures. Second, and less intuitively, the kinetic inductance of the detector increases as a result of pair-breaking. Because there are now few charge carriers available to sustain the superconducting current excited by the feedline, the kinetic energy of each pair must increase, and with it the lag between driving current and charge carrier motion. This increased inductance decreases the device's resonant frequency, which manifests in Figure 2b as a leftward shift in notch position. The quantitative nature of these resonance behavior changes is laid out below.

2.1 Resonance Behavior

The total MKID inductance L is simply the sum of its geometric inductance L_g and kinetic inductance L_k, or

$$L = L_g + L_k \tag{1}$$

The kinetic inductance fraction α is defined as

$$\alpha = \frac{L_k}{L_k + L_g} = \frac{L_k}{L} \tag{2}$$

In most MKIDs, the geometric inductance is much larger than the kinetic inductance, and consequently α is small. The exact value of α depends on the designs of the resonator and the feedline, and is typically computed numerically.

The total surface impedance of the thin superconducting film is related to the total inductance by

$$Z_s = R_s + iX_s = R_s + i\alpha\omega L \tag{3}$$

where X_s is the surface reactance and R_s is the surface resistance due to the quasiparticle density. These quantities determine the resonant frequency ω_0 and internal quality factor of the resonator Q_i as follows:

$$\omega_0 = \frac{1}{\sqrt{LC}} \tag{4}$$

$$\frac{1}{Q_i} = \frac{R_s}{\omega L} = \alpha\frac{R_s}{X_s} \tag{5}$$

Similar to the inductance, the total quality factor Q_r of the resonance is split into two factors: the internal quality factor Q_i and the coupling quality factor Q_c describing the energy loss between resonator and feedline.

They add in parallel:

$$\frac{1}{Q_r} = \frac{1}{Q_c} + \frac{1}{Q_i} \tag{6}$$

This definition of quality factor is simply the ratio of power stored in the resonating system to power dissipated every cycle by the system. Higher values indicate less dissipation, more energy stored, and therefore higher energy drop in the feedline. The exact relationship is well-described by the single-pole approximation [3]:

$$S_{21} = 1 - \frac{Q_r}{Q_c} \frac{1}{1 + 2iQ_r \frac{\omega - \omega_0}{\omega_0}} \tag{7}$$

This shows that larger quality factors correspond to deeper and narrower notches in measurements like Figure 2b, with the notch centered on resonant frequency ω_0. Now that the measurable quantity, the frequency response curve of S_{21}, has been related to the properties of the MKID, the next step is to determine the effect an energy deposition has on the shape of that curve.

2.2 Quasiparticle Effect

Both Q_i and ω_0 are sensitive to the quasiparticle density inside the superconducting film. That quasiparticle density is effected by two factors: the non-zero temperature of the superconductor and the total rate of incident pair-breaking events. The first factor can be treated as effectively constant for the purposes of analyzing MKID responsivity. The second is responsible for the MKID's utility as a detector.

Relating the change in quasiparticles due to pair-breaking to a change in the surface impedance involves analysis of the full Mattis-Bardeen complex conductivity, which is beyond the scope of this thesis. From [4], in the low-temperature, low-frequency (less than X-ray) and low-occupation limits,

$$\frac{\delta Z_s}{|Z_s|} = \kappa |\gamma| \delta n_{qp} \tag{8}$$

where n_{qp} is the number density of quasiparticles, γ is a numerical constant ranging from $-1/3$ to -1 depending on the thickness of the film and κ is a complex temperature-dependent value describing the fractional dependence of complex conductivity on n_{qp}. Determining the full value of κ involves solving the Mattis-Bardeen integrals for complex conductivity in the limits listed above; for the purposes of characterizing trends in MKID behavior, it is sufficient to note that both its real and imaginary parts are always positive. This fact, combined with the absolute value sign around γ, shows that both parts of the complex Z_s increase when the number of quasiparticles increases.

This information is sufficient to determine the trend of ω_0 and Q_r in response to changes in quasi-particle density. The changes of those parameters in terms of $Z_s = R_s + iX_s$ according to Equations 4 and 5 are

$$\frac{\delta \omega_0}{\omega_0} = -\frac{1}{2}\frac{\delta L}{L} = -\frac{\alpha}{2}\frac{\delta L_k}{L_k} = -\frac{\alpha}{2}\frac{\delta X_s}{X_s} \tag{9}$$

$$\delta \frac{1}{Q_r} = \delta \frac{1}{Q_i} = \alpha \left(\frac{\delta R_s}{X_s} - \frac{R_s \delta X_s}{{X_s}^2} \right) \simeq \alpha \frac{\delta R_s}{X_s} \tag{10}$$

Here, the last expression can be simplified because, in the limit $T \ll T_c$, X_s is much larger than both R_s and δX_s. Then, because δR_s and δX_s are simply the real and imaginary parts, respectively, of δZ_s, combining Equations 8 through 10 yields

$$\frac{\delta\omega_0}{\delta n_{qp}} = -\frac{\alpha}{2} Im(\kappa)|\gamma|\frac{\omega_0}{X_s} \tag{11}$$

$$\frac{\delta\frac{1}{Q_i}}{\delta n_{qp}} = \alpha|\gamma|\frac{Re(\kappa)}{X_s} \tag{12}$$

These relations can easily be put in terms of the total energy absorbed E, because each energy input equal to the gap energy Δ produces two quasiparticles:

$$\frac{\delta\omega_0}{\delta E} = -\frac{\alpha}{4\Delta} Im(\kappa)|\gamma|\frac{\omega_0}{X_s} \tag{13}$$

$$\frac{\delta\frac{1}{Q_i}}{\delta E} = \frac{\alpha}{2\Delta}|\gamma|\frac{Re(\kappa)}{X_s} \tag{14}$$

Consequently, in response to an increase in quasiparticle density, ω_0 and Q_r (through Q_i) will both decrease, as shown previously in Figure 2b. This is then linked to the sensitivity of the entire detector through the measured transmission parameter S_{21}. Its response to a pair-breaking event around the resonance frequency can be found by differentiating Equation 7:

$$\delta S_{21}|_{\omega=\omega_0} = \frac{{Q_r}^2}{{Q_C}^2}(\delta\frac{1}{Q_i} - 2i\frac{\delta\omega_0}{\omega_0}) \tag{15}$$

This shows that the change in transmission behavior is proportional to the square of the overall quality factor. Thus, any decrease in an MKID's Q factor can significantly decrease its sensitivity as a detector; it is this fact that motivates the filter construction detailed in the following chapters. However, it should be noted that there are some design constraints that motivate having a finite Q. Most importantly, the feedline power itself breaks a number of Cooper pairs during readout, proportional to the power of the feedline signal and the overall quality factor of the resonator [5]. Past a certain density, these quasiparticles will substantially decrease the internal quality factor, an effect that sets an upper limit on readout power. Working in the other direction, the overall readout noise is typically dominated by the post-device low-temperature amplifier (see the next subsection), which has noise inversely proportional to the readout power.

Together, these two competing effects define an optimum readout power that minimizes amplifier noise while also not creating too many temporary quasiparticles; the value of this optimum power is proportional to $\frac{Q_c}{{Q_r}^2}$ [5]. Combined with Equation 15, [5] finds that sensitivity is maximized when $Q_c \approx Q_i$. Thus, efforts to improve overall MKID sensitivity should increase both Q_i and Q_c simultaneously. The first effort motivates most of the activity in this thesis, while the latter effort involves the patterning and design of the MKID chip itself, which is beyond the scope of this work.

2.3 MKID Readout Electronics

Reading out the properties of an MKID detector requires a dedicated but fairly simple chain of readout electronics shown in Figure 3. The most complicated electronics, the DAQ computer and software-defined radio (SDR), both sit at room temperature. The SDR is connected to both ends of the data line, so it generates the initial feedline signal and reads out the resulting output signal to calculate S_{21}; the Ettus X310 model (with a daughterboard installed to extend the frequency range) was used for readout purposes in the course of this investigation. The SDR is controlled by a server running on the graphics card of the DAQ, through which a wide array of measurement scripts and protocols can be executed [6].

The data line itself is a simple SMA line that runs through each temperature stage of the fridge, connects to the input of the on-chip feedline, connects to that same feedline's output, then runs back up to room temperature. The temperature stages shown in Figure 3 are fairly typical. On the input side, an attenuator is placed at 3K to prevent the large powers generated by the room-temperature SDR from overloading the cryogenics. Then, an amplifier is placed on the output side at 3K; without it, the resonance characteristics of the MKIDs would be overwhelmed by the thermal noise contributed by warmer temperature stages.

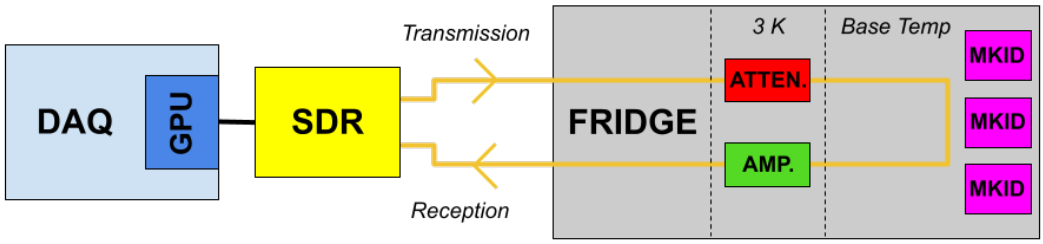

Figure 3: Schematic of the readout electronic system used for this investigation. "ATTEN." is short for attenuator, "AMP." is short for amplifier. The value of the attenuation was ∼20 dB and the value of the amplification was ∼40 dB.

The previous section showed that, in general, higher quasiparticle densities reduce the detector's sensitivity, creating an incentive to minimize the number of quasiparticles in the superconducting film. This readout scheme presents an obvious obstacle to that minimization; the necessary injection of a signal on a continuous data line running from room temperature all the way to the device's location at base temperature. General-purpose attenuators like the one used here have no effect on frequencies as high as the infrared, so the feedline effectively acts as a path for blackbody radiation generated at every temperature above base to reach the detector chip. Regardless of the specific superconducting material being used in an MKID, the majority of infrared photons will have energy greater than or equal to twice the gap energy Δ and consequently any that reach the detector will be able to generate quasiparticles in the substrate. Finding a way to filter out these infrared photons then presents an opportunity for substantial MKID performance improvement.

3 ECCOSORB Filters

While some population of quasiparticles is inescapable at any temperature above absolute zero, an appreciable fraction of those present at experimental temperatures are generated by the background level of incident photons. Thus, any efforts aimed at increasing MKID sensitivity should include strategies for better insulating the superconducting film from any photons energetic enough to break Cooper pairs. Light-tight detector shielding can minimize the incidence of optical and higher-frequency light, but the data readout lines (shown above) must necessarily pass through such shielding and provide a path for infrared photons to reach the detector from warmer stages of the refrigerator. The most natural solution is to place filters on the data transmission line, generally at the 3K stage or below, to block these infrared photons,

Unfortunately, small inline filters with the electrical characteristics necessary to block infrared photons are not currently commercially available at the required specifications. In response, many laboratories have landed on a semi-commercial solution: injecting a proprietary loaded epoxy compound, ECCOSORB CR, into a variety of custom filter enclosures. ECCOSORB is designed to absorb microwave frequencies, but this attenuation continues far past the region necessary for IR-filtration; when cured, it is optically opaque. The next sections detail the design of a custom filter enclosure for use in MKID readout.

3.1 Design

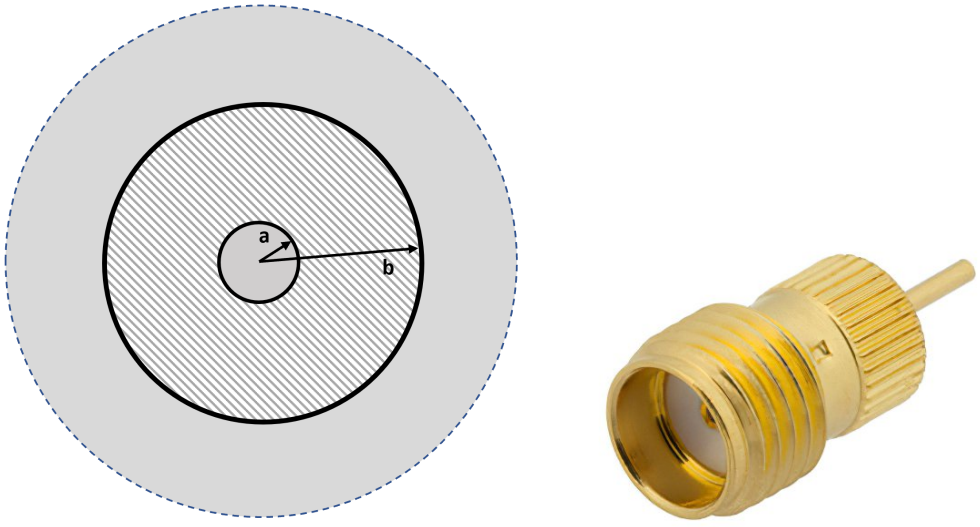

Figure 4: a (left): Cylindrical cross section of basic ECCOSORB filter design. The dashed portion represents epoxy, while shaded represents a conductor (typically copper). b (right): Pasternak PE44241 press-in SMA connector used at each end of a filter cavity.

The core concept for creating an epoxy filter has remained relatively unchanged for more than a decade [7]. It is based on a coaxial design, with the dielectric epoxy separating the inner and outer conductors as

shown in Figure 4a. The radii of the inner conductor (a) and outer conductor (b) determine the passband range of the filter, which should be 4 - 8 GHz for most relevant MKIDs. The length of the coaxial segment determines the overall attenuation of the filter; longer sections of epoxy lead to a more attenuated signal. For this application, shorter lengths are generally chosen to maximize transmission in the passband. Typically, each end of the coaxial segment is terminated by a female SMA connector whose pin forms the center conductor, fixing the value of a at 0.03in (Figure 4b).

Typical Electrical Properties

	GHz	10^{-7}	10^{-6}	10^{-5}	10^{-4}	10^{-3}	10^{-2}	10^{-1}	1.0	3.0	8.6	10.0	18.0
MF-110	K'	18	16	15	13	11	9	7	5	3.2	3	2.9	2.8
	tan δ_d	0.01	0.01	0.02	0.02	0.03	0.03	0.04	0.04	0.05	0.05	0.04	0.04
	K"	0.18	0.16	0.3	0.26	0.33	0.27	0.28	0.2	0.16	0.15	0.12	0.11
	M'	1.2	1.2	1.2	1.2	1.2	1.2	1.1	1.1	1.1	1	1	1
	tan δ_m	0	0	0	0	0	0	0	0	0	0.1	0.1	0.2
	M"	0	0	0	0	0	0	0	0	0	0.1	0.1	0.2
	dB/cm	0	0	0	0	0	0	0.01	0.09	0.26	2	2.2	6.6
	dB/in	0	0	0	0	0	0	0.03	0.23	0.66	5	5.6	17
	$\lvert Z\rvert/Z_0$	0.26	0.27	0.28	0.3	0.33	0.37	0.4	0.47	0.59	0.59	0.59	0.6

Figure 5: Frequency dependent electrical properties of the machinable ECCOSORB epoxy stock MF-110, identical to those of the castable product CR-110. Here, K' and K" are the real and imaginary parts of the permittivity, and M' and M" are the real and imaginary parts of the magnetic permeability.[8]

The ideal outer radius b for minimizing reflection in the 4 - 8 GHz range was found in [9] by calculating the impedance of a dielectric-filled coaxial cable using

$$Z = \sqrt{\frac{\mu_0}{\epsilon_0}} \sqrt{\frac{\mu_r(1 - i\tan\delta_m)}{\epsilon_r(1 - i\tan\delta_d)}} \ln\frac{b}{a} \tag{16}$$

where relative permeability μ_r, relative permittivity ϵ_r, magnetic loss tangent δ_m and (di)electric loss tangent δ_d are known frequency-dependent quantities of the specific epoxy mix used in this filter, ECCOSORB CR-110, given in Figure 5. Then, the value for the outer radius that minimized the impedance mismatch between Z and the standard 50Ω SMA cable in the operating range was found to be $b = 0.125in$.

With these dimensions in hand, several designs (Figure 6) were created by modifying an existing filter design supplied by Robert McDermott's group out of the University of Wisconsin (full drawings can be found in Appendix A). Both include a central cavity meant for filling with epoxy and holes on each side of that chamber for the SMA connectors to be inserted into, as well as a hole (termed the "filling hole") at the top of the epoxy chamber through which the two SMA connectors are soldered together and the epoxy is subsequently poured. The first design, known as the "box" design, was designed to screw on to an adapter plate at the mixing chamber stage of the fridge housing the MKIDs. The second design is shaped hexagonally and intended to hang from the SMA data line it is filtering. A hexagonal exterior was chosen over a circular exterior to make it easier to screw connections on and off from the SMA connectors on each side of the filter. Drawings for each can be found in Appendix A.

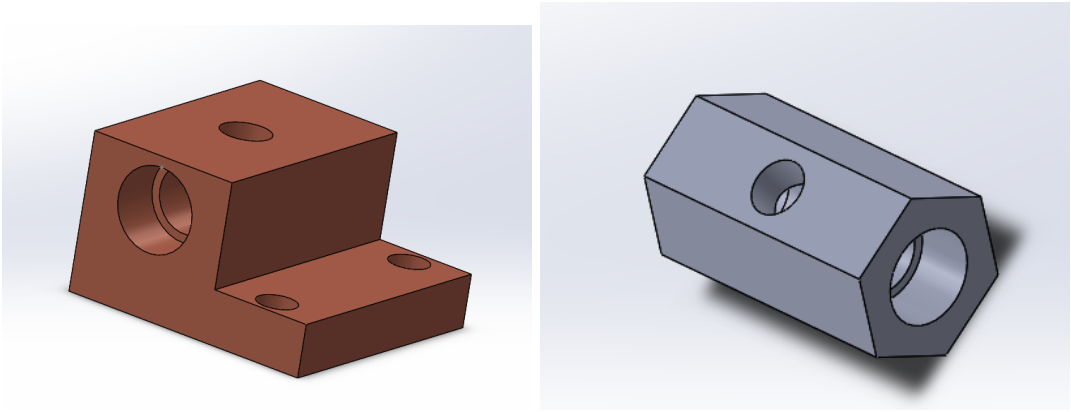

Figure 6: a (left): Two designs for the exterior shape of the epoxy filters, showing the holes at the ends for the SMA connectors, and the filling hole in the top. The cavity where the epoxy is poured into has a slightly smaller radius than the connector holes, and is partially visible in both designs.

At this point, two main questions about the design remained. The first was whether altering the outside shape of the filter might have adverse impacts on the filter's performance. The second was whether changing the length of the coaxial segment (equivalently, the length of the cavity filled with epoxy) might provide an avenue for further improving its performance. The length of the designs shown in Figure 6 were partially set by the length of the SMA connector pins (Figure 4b), which meet in the middle just under the filling hole with a small gap left between for soldering. However, if a different length produced significantly better electrical performance, namely higher transmission and lower reflection in the 4 - 8 passband region, altering the length of these pins might be a cumbersome but worthwhile step of the assembly process.

3.2 Simulation

In order to explore the effect of changing different parameters such as overall length and filter shape, various designs were simulated in the finite element solver HFSS. The simulation of the hexagonal filter is shown in Figure 7a. The material properties provided by the epoxy manufacture (Figure 5) were programmed in, along with those for copper (for the filter bodies), Teflon, brass, and gold (for the SMA connectors). Then, two wave port excitations were applied to each end of the coaxial segment (Figure 7b). The solver assumes that each port connects the filter to a semi-infinitely long waveguide that has the same cross-section and material properties as the port; the outside edge of the port defines the ground plane (in this case the filter exterior) and the inside edge outlines the signal conducting volume (in this case the conducting pins). The excitation input impedances were set to 50 Ω to match that of a standard SMA cable, and the excitations' frequencies were varied from 0 to 30 GHz. The voltages resulting from each excitation were measured at both the exciting port (to calculate reflection) and the port on the opposite side (to calculate transmission). Therefore, the S_{21} term represents the ratio of voltage observed at port 2 due to voltage created at port 1, the S_{22} term represents the ratio of voltage observed at port 2 due to voltage created at port 2, and so on.

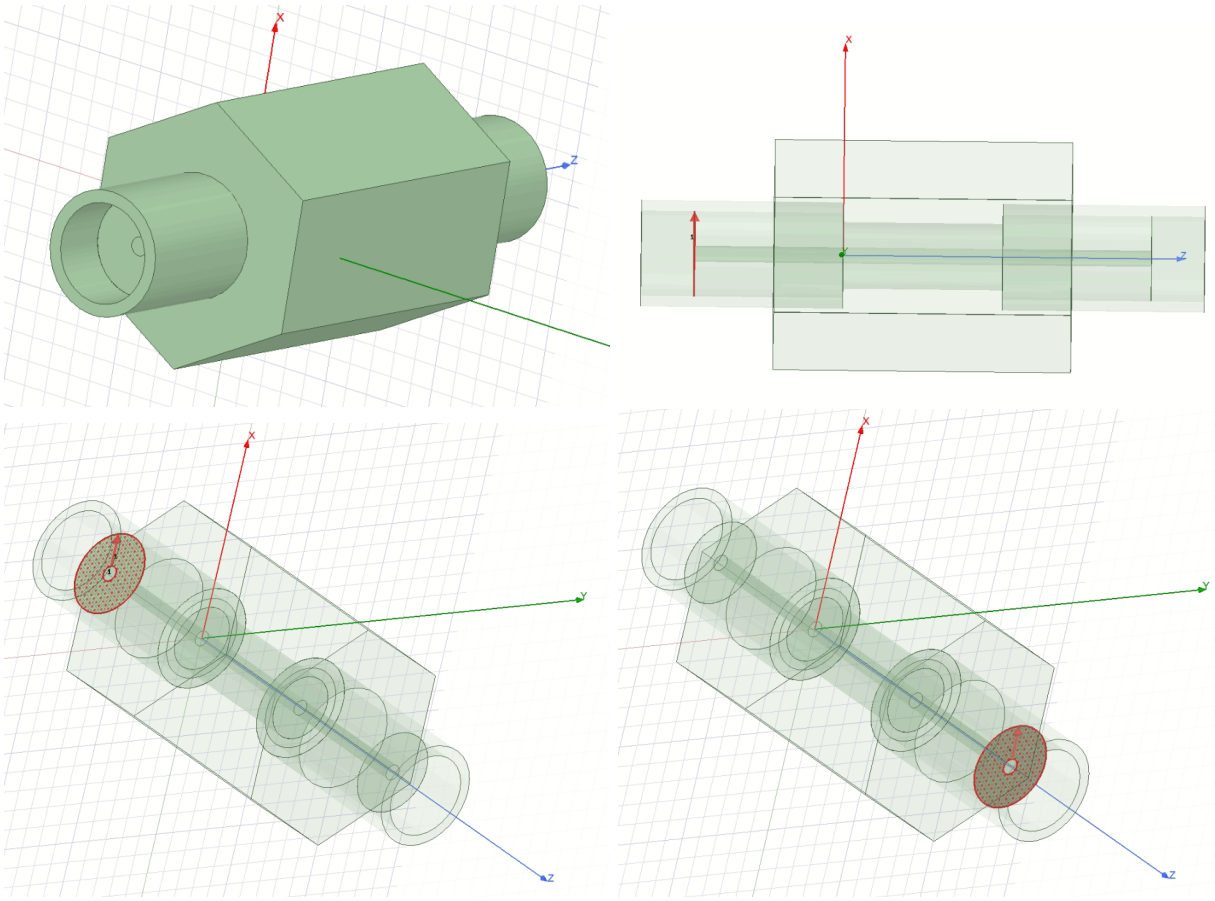

Figure 7: a (top row): Isometric view and cross-section of the hexagonal filter model created in HFSS. b (bottom row): The excitation locations on the filter model.

Three different filter shapes were tested: box, circle, and hex, with their models following the coaxial shape of Figure 4a with different shapes replacing the dashed outer circle. The goal was to determine whether the outside shape could be modified to fit different applications without significantly affecting the electrical performance of the filter. The results are displayed in Figure 8, and show that the outside filter shape had very little impact on the transfer functions. The transmission is effectively identical for all three shapes at all frequencies. The magnitude of the reflection varies slightly between the three shapes at a few frequencies, but its shape remains constant. At a practical level, this data implies that changing the outside shape of the filter will not have significant consequences on filter performance.

Some interesting features do jump out from this first set of transmission and reflection curves. First, the sum of the two is not equal to 0 dBm across all frequencies as one might initially expect, but is instead always < 0 dBm and varies across the frequency range. This behavior can be attributed to the effects of dielectric (and to a lesser extent magnetic) loss. Those values become significant at higher frequencies (Figure 5, the same range where the difference between the coefficient sum and unity is most pronounced. Second, the transmissions measured in opposing directions (S21 and S12) through the filter are identical, while the

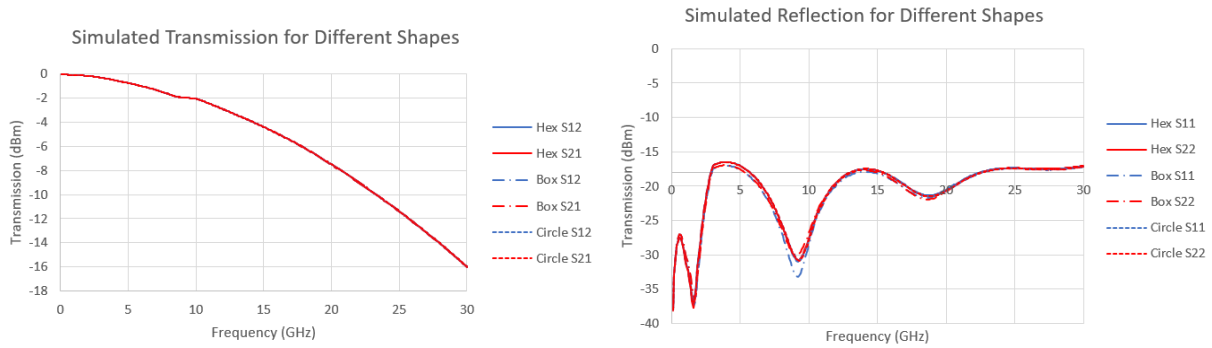

Figure 8: Transfer functions for three different modeled outside filter shapes: box, circular, and hexagonal.

reflections measured at each end (S11 and S22) for the box differ slightly. Reflecting the measurements across the filter's midpoint shouldn't effect these values, because it is symmetric through that plane. Therefore the transmission is behaving as expected, but the reflection is producing some small anomalies. This is most likely due to the error introduced by the finite element solving method; specifically, one end of the filter was placed at the origin (Figure 7), so each end is treated slightly differently by the simulator even though they are physically identical. This effect is most pronounced for the box filter likely because it has the least symmetric cross-section, and is thus more difficult for the simulator to solve.

Following the shape study, the full version of the filter (with the outer shape arbitrarily chosen to be the box) was modeled in HFSS, including the SMA connectors pressed into each side and their accompanying Teflon dielectric. Then, the length of the filling cavity in the center of the filter was varied around the initial value of 0.365in (determined by the SMA pin length). The results are shown in Figure 9, and clearly demonstrate that the filling cavity length affects both the transmission and reflection characteristics of the filter. Shorter lengths correspond to higher transmissions, which makes intuitive sense given that longer lengths lead to larger attenuations. The shift in harmonic reflection behavior between filters of different lengths was more of a surprise, as the length of the filter appears nowhere in the theoretical impedance expression for a coaxial filter (Equation 16). However, its clear that shorter filling lengths shift the reflection peaks and troughs towards higher frequencies.

Overall, the numerical differences in performance are small between filters with different filling lengths. The increase in transmission from shortening that length amounts to a fraction of a decibel in the range of operating frequencies, and the shifts in reflection behavior aren't particularly advantageous or disadvantageous within that same range. Because of this, it was decided to stick with the original filling length of 0.365in. The specific reasoning was that the process of shortening the SMA pins to accommodate a shorter filling length would be difficult, time-consuming, and likely to create imperfections that would offset any increases in performance due to the change. That decision completed the list of the most important dimensions used in the final filter designs; a short summary is provided below.

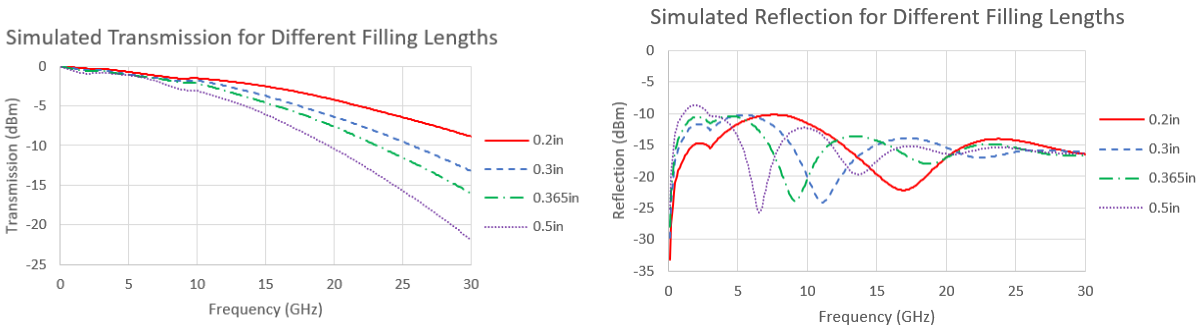

Figure 9: Transfer functions for four different filling cavity lengths, simulated through a fully modeled box-type filter. S21 is used for transmission and S11 for reflection to improve visibility; however, these values are visually identical to S12 and S22, respectively.

Inner Conductor Radius a	Outer Conductor Radius b	Filling Length
0.03in	0.125in	0.365in

3.3 Improvements

Following the construction of an initial batch of these filters, it was decided that the hex form-factor filters were more versatile than the box type, because they didn't need an adapter plate to mount into a fridge, and so the main production batch consisted entirely of hex filters. Additionally, a sloped edge was added to the filling hole in order to address problems with adding the epoxy to the filling cavity, covered in the following assembly section. Finally, the jigs for inserting the SMA connectors into the filter bodies were significantly overhauled in order to address problems with SMA pin alignment inside the filling cavity, also covered in the following section.

For the future, multiple avenues for filter design improvement exist. Currently, both ends of the filter terminate in female SMA connections, which necessitates use of a female-to-female adapter when placed inline on the feedline (visible in Figure 17). Ideally, one end of the filter should terminate in a male SMA connector: however, no such connector meeting current assembly requirements (knurled for pressing, includes solder pin) is available online at the time of writing, but it's possible one could be manufactured in-house. Additionally, work should also continue on implementing the current filter design as a mounted feedthrough between different fridge temperature stages. While this idea in the form of the box filter was abandoned in favor of versatility, it does offer advantages for experiments running long-term with the same setup and hardware. Finally, future designs could also delve deeper into the possibilities of changing the coaxial length of the filter to achieve higher transmission in the passband.

4 Filter Assembly

There are three main steps in assembling an ECCOSORB filter. First, the knurled SMA connectors are pressed into each end of the filter enclosure. Then, the ends of the connector pins are soldered together, completing the inner conductor portion of the coaxial filter design. Finally, the cylindrical cavity around the pins is filled with liquid epoxy and cured. The materials required for this process are the elements displayed in Figure 10, along with solder paste and the two-part ECCOSORB CR-110 ingredient kit (Part X and Part Y). The following laboratory tools are also necessary: bench vise, multimeter, soldering iron, hot plate, scale, standard weighing tins, mixing sticks, plastic pipettes, vacuum chamber, and oven. A fume hood or other ventilation method is recommended for all steps that involve heating epoxy.

4.1 Pressing

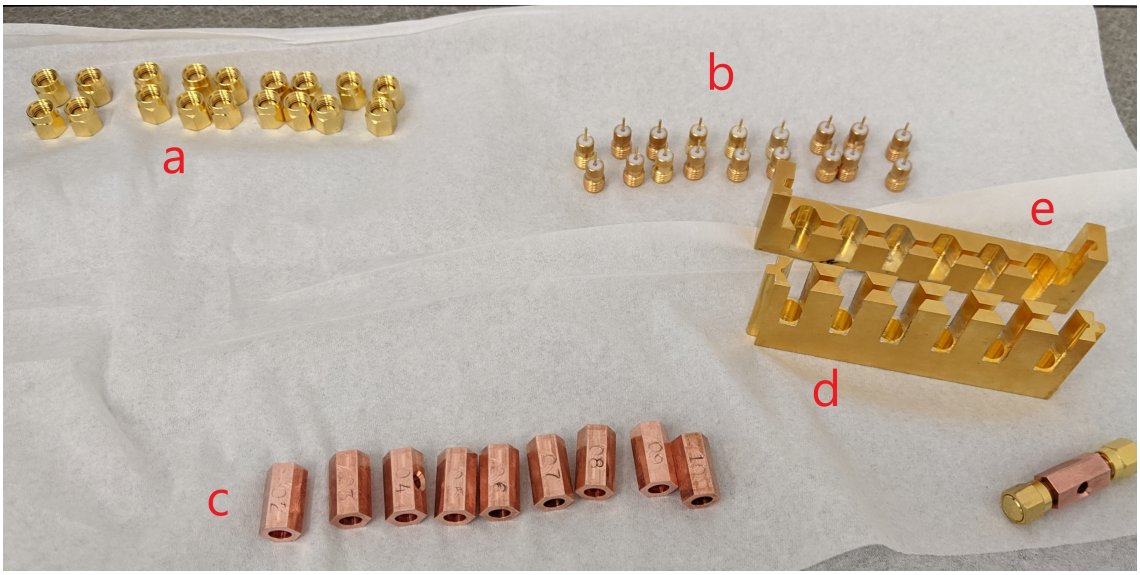

Figure 10: Materials for the pressing stage. a) Amphenol 202112 SMA caps. b) Pasternak PE44241 knurled press-in SMA connectors. c) Custom hex-form copper filter enclosures. d) Hex filter pressing jig. e) SMA connector pressing jig. A fully pressed filter sits in the lower right.

In this stage, the knurled SMA connectors (10a) are inserted into each end of the filter enclosure (10b) using a bench vice. Pressing (instead of gluing, soldering, or screwing) is required to make sure the filling cavity is absolutely sealed on the sides; otherwise, the epoxy will completely drain during the curing process.[1] During the pressing process, a pair of jigs (10c) are used to correctly align the connectors and the enclosures. They ensure that the inner pins remain coaxial. Pins that aren't aligned with each other can degrade the

[1] One filter that developed a hairline crack during pressing was filled with epoxy and placed in the curing oven. After curing, all epoxy had drained out of the filing cavity, gluing the filter to the surface it had been placed on and rendering it effectively useless.

filter's performance, and in severe cases cannot be soldered together.

The first step in the pressing stage is to wipe down the filter enclosures, connectors and caps with a solvent such as IPA. Then, prepare the SMA connectors by screwing caps on to protect their threading during the entire construction process. Place a small dab of solder paste on the end of each connector's pin as shown in Figure 11b. Not much is needed, and it's important to make sure paste doesn't stick far enough to the side to touch the filter wall later and potentially cause a short.

For the pressing itself, insert up to two enclosures into the longer jig. Although the jig has space for eight enclosures, it was discovered during testing that the pressure involved in simultaneously pressing connectors into that many enclosures was dangerous for the enclosures themselves and occasionally cracked them. Insert them with their filling holes visible (Figure 11a); this is useful for knowing how far to press each connector.

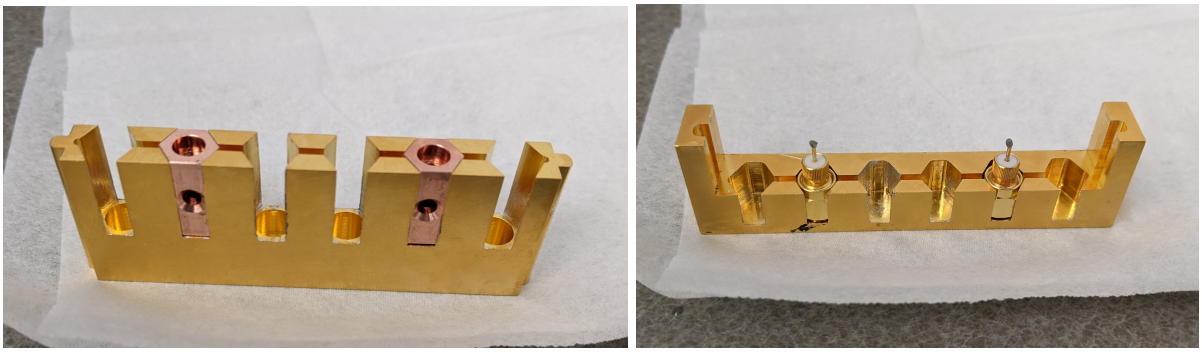

Figure 11: a (left): Enclosures correctly inserted into hex jig. b (right): SMA connectors prepared for pressing with cap and solder paste.

Insert SMA connectors into the corresponding slots on the smaller jig (Figure 11b). Slide the two jigs together using the tab and groove system, and secure on the bench vise as shown in Figure 12a. Depending on the type of vise, it may be necessary to elevate the entire assembly up off of the base to ensure that the top and bottom edges of the jigs are feeling equal pressures. Then, slowly press the connectors into the filter enclosures, checking to make sure none of the connectors have skewed off-center. This is important because pressing is a non-reversible process, and an enclosure with an improperly inserted connector is often unusable. Stop pressing when the knurling at the top of the connector body is almost or completely inside the filter enclosure. At this point, the solder paste at the end of each connector pin should occupy roughly the center of the filling cavity as judged through the filling hole. Some connectors may have become more inserted than others due to small variations in size or fit into the jigs; this problem can be corrected by either intentionally placing the assembly off-center in the vice to apply more pressure to one side or by finishing the press for individual filters without the jigs.

Now, take the half-pressed enclosures out of the jigs. Temporarily remove the SMA caps, reverse the enclosures and reinsert them into the pressing jig. Add new SMA connectors to the smaller jig and insert them into the enclosures as before; the only difference is to stop pressing when the solder paste of each pin

Figure 12: a (left): Filter and connector inserted into jigs and being pressed by bench vise. b (right): A filter that's been pressed from both sides; solder paste from each pin has joined in the middle.

has met and compacted in the middle of the filter, as shown in Figure 12b. With solder paste of sufficient quality, the connectivity of the inner conductor can be verified with a multi-meter before proceeding. After removal from the jigs, each filter enclosure should be marked with a number and other relevant details such as construction date or inner radius size. Stamping is recommended over engraving because the curing process can make the latter unreadable.

4.2 Soldering

At this point, the filter enclosure should like the example given in 13a, with soft paste filling the small gap between the pins of the SMA connectors. The goal of this step is to complete the electrical connection between the two pins without shorting to the outside wall of the filter. Select a solder iron with a tip wide enough to touch both connector pins simultaneously, and heat it to 600F. [2] The filling hole is not large enough to see through when the solder iron is inserted through it, so the soldering itself must be done blind.

Insert the iron through the filling hole and lever against the tips of both connector pins. Hold in place for five seconds, then remove. A cleanly soldered connection is displayed in Figure 13b. Check with a multimeter to make sure that the resistance between the center pins is less than 1Ω and that there is no connection between the inside pins and the surrounding copper of the filter body.

Filters that fail one of these criteria can often be repaired using a variety of techniques. For instance, if all the solder paste has solidified but the resistance between the pins is still too high, it's possible to add additional paste through the filing hole with tweezers. Solder this additional paste, re-check the connection and repeat this process as necessary. If instead the solder has caused a short by bridging the gap from the pins to the side wall, it's frequently possible to break this undesirable connection using a pair of hooked

[2] This section assumes the use of high-quality silver-bearing solder paste. Lower-quality paste will not conduct at all when un-soldered, and splatters when contacted by a 600F solder iron. Instead, use a 450F iron and hold for ten seconds.

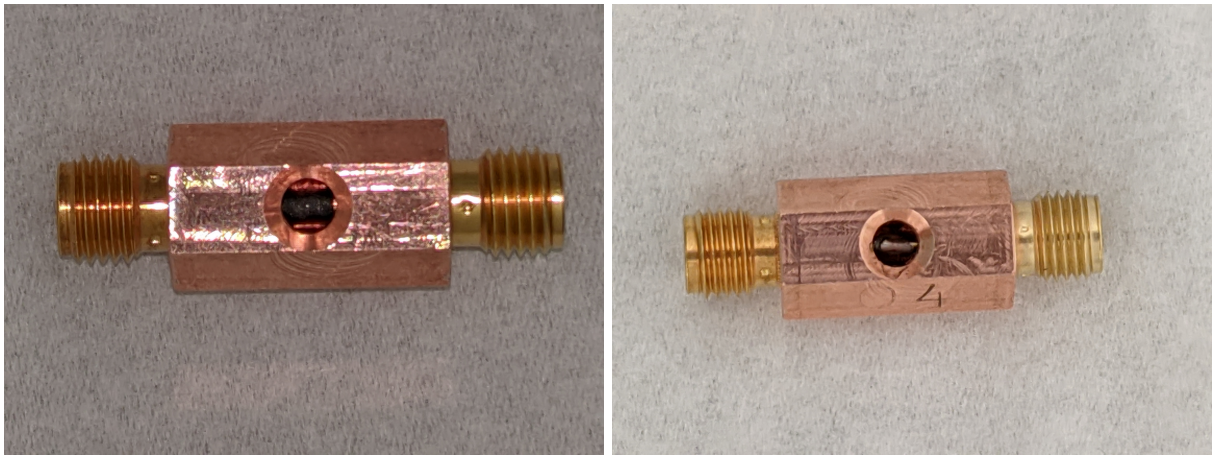

Figure 13: a (left): Fully pressed filter with unsoldered paste connecting the two SMA connector pins. b (right): The same filter after the paste has been soldered.

tweezers or a similar tool. Once the filter is functioning correctly as a coaxial connector, it's ready to be filled with ECCOSORB epoxy.

4.3 Filling and Curing

The two main ingredients of ECCOSORB CR epoxy are called Part X and Part Y. Part X is a viscous glue that forms the majority of the epoxy by volume, while Part Y is a liquid loaded with metal filings that give the epoxy its dielectric properties. The epoxy is prepared by heating, mixing and degassing these ingredients[3]. It is then poured into the filter cavities and cured in an oven.

The first step is to stir the Part X in its container using mixing sticks until it appears homogeneous. Then, weigh out 100 parts of it onto a weighing tin; ten grams proved to be an appropriate amount for filling ten filter enclosures. Heat on a 65C hot plate for five minutes, then add 12 parts of Part Y using a pipette. The mixture should look like Figure 14a. Mix unheated for another five minutes to make the epoxy appear homogeneous. Finally, place the mixture in vacuum for 10 minutes. This degasses the epoxy, preventing air bubbles from forming during the curing process that would degrade electrical performance (Figure 14b).

To actually fill the filters with the epoxy, preheat both the epoxy and the enclosures at 80C on the hot plate (Figure 15a). This will make it easier to work with the epoxy by decreasing its viscosity, but it does set an upper bound of roughly an hour before the epoxy will begin setting. Fill a pipette with epoxy and place it at a very flat angle with respect to the filter itself, as shown in Figure 15b. Slowly add epoxy to the rim of the filling hole, allowing it to drop into the filter cavity by itself. Keep adding epoxy like this until the cavity is full.

One major obstacle during this step is the formation of epoxy bubbles over the filling hole while the

[3]In order to prevent the build-up of epoxy fumes, use of sufficient ventilation (fume hood, positive-pressure cleanroom) for all heating steps is recommended

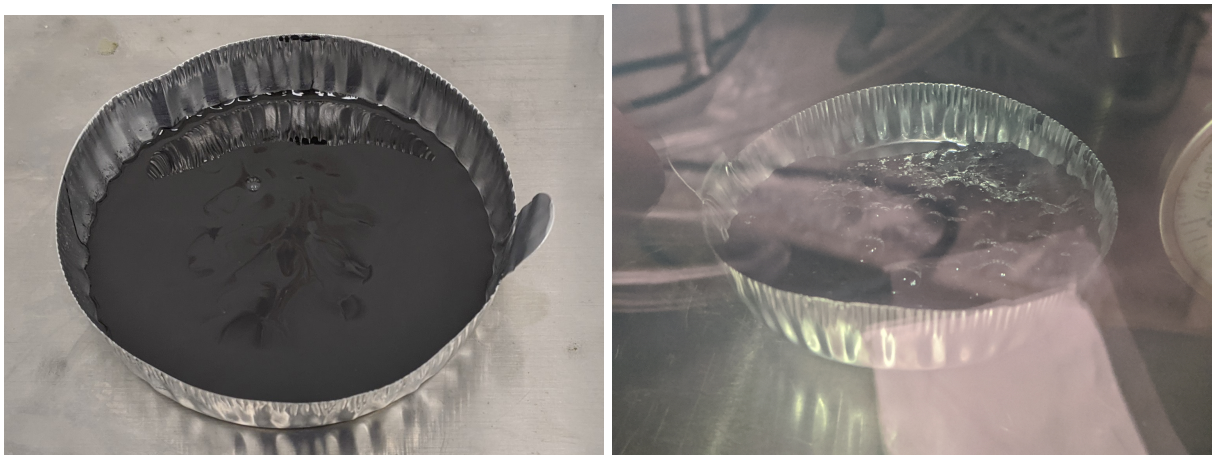

Figure 14: a (left): Epoxy immediately after the addition of Part Y. b (right): Air bubbles leaving the epoxy as it sits in vacuum.

cavity is still unfilled. Slow, angled application of the epoxy reduces but does not completely eliminate this problem; employ tweezers to poke and remove material from bubbles until they pop. Additionally, epoxy bubbles can be difficult to visually distinguish from a truly filled cavity. A good visual cue is to watch for the soldered pins being slowly submerged by the rising epoxy; this proves the cavity is actually filling instead of just being obscured by a bubble around the filling hole.

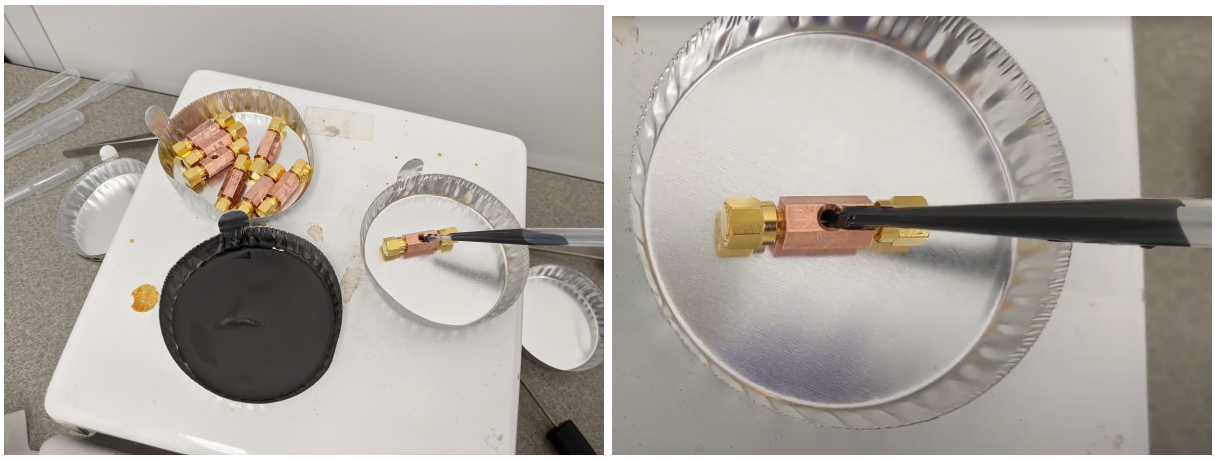

Figure 15: a (left): Filters and epoxy preheating on hot plate. b (right): Closeup showing angled insertion of epoxy.

When all filters are satisfactorily filled, carefully remove any epoxy that has made its way to the edge of a filter body near the SMA connector threading. This material can glue the caps onto the connectors, making it extremely difficult to remove them after curing. Then place the filters into a 93C oven for 4 hours to cure.[4] Also cure a small epoxy sample of the epoxy by itself for verification that it has fully set.

[4]This is the fastest curing schedule that avoids melting the dielectric component of the SMA connectors.

5 Results

5.1 Typical Filter Performance

The transfer functions of each filter were measured individually up to 20GHz using a network analyzer. The results for four characteristic filters are displayed in Figure 16 (all other transfer function plots are available in Appendix B). The transmission behavior (labeled "S21" and "S12") didn't have significant variance between filters. With few exceptions, each had a fairly linear frequency dependence with a slope varying between -0.2dB/GHz and -0.4dB/GHz. In the intended operational range of 4 - 8 GHz, transmission varied little between -2 and -3 dB.

By contrast, the reflection (labeled "S11" and "S22" on the graphs) followed a harmonic profile, generally staying below -20 dB from 0 - 6 GHz and rising past -15 dB at higher frequencies. Many filters had a reflection minima between 4 and 6 GHz, reflecting the design goal of the outer radius calculated by [9]. Beyond these characteristics, the shape and amplitude of reflective behavior varied noticeably from filter to filter, with some, like 04, relatively having flat profiles and others such as 13 having far more frequency dependence.

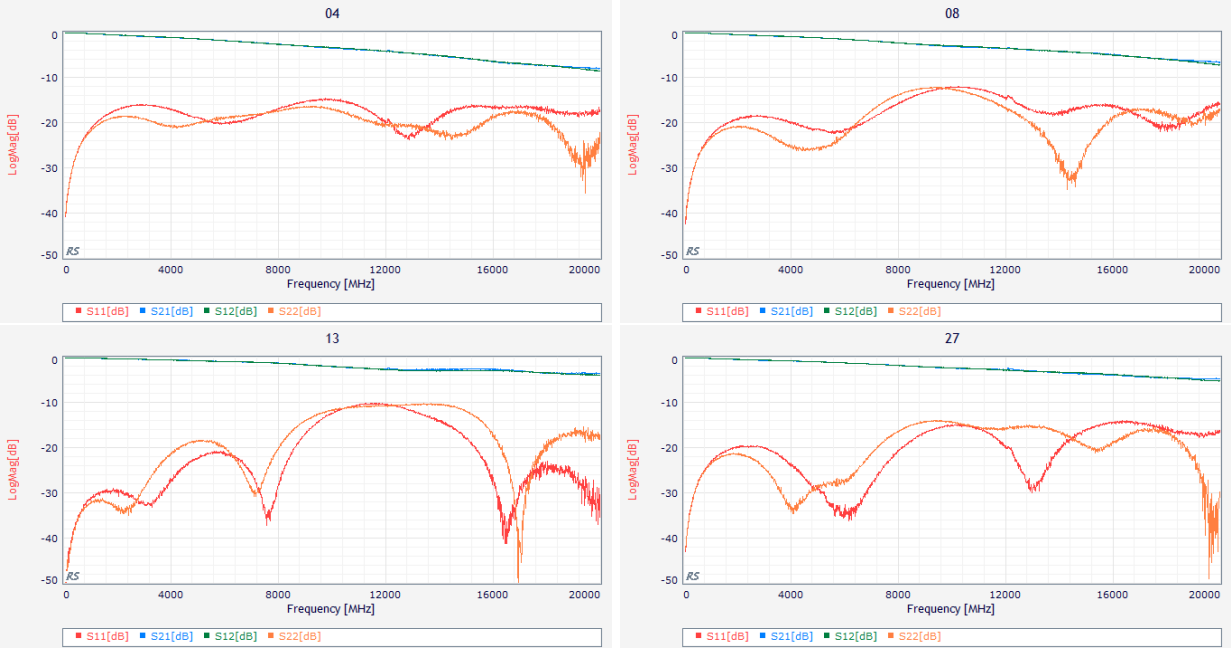

Figure 16: Transfer functions of 4 filters, selected to represent the characteristics of the final batch. The lower red and orange lines show reflection behavior, the upper blue and green lines show transmission behavior. Filter numbers, clockwise from top left, are 04, 08, 13 and 27.

Based on these results, most importantly high transmission and low reflection at the operating frequency of 4 GHz, most filters were considered suitable for placement inline on the MKID feedlines. One interesting takeaway from the variability of the reflection behavior is that different filters may be better suited for some experiments than others. For example, an experiment that's only interested in transmitting signal at 2 GHz

would prefer filter 13 because of its very low reflection (roughly -30dB) at that frequency. However, using filter 13 in an experiment that required signal transmission at a wide range of frequencies might pose an issue because of its relatively higher reflection (-10 dB) at higher frequencies; such an experiment would prefer the flat profile of filter 04 that never rises above -15 dB.

5.2 Effect on MKID Behavior

Several filters, produced in the batch pictured above, were tested on the Al resonator (shown in Figure 2) which was then installed in an adiabatic demagnetization refrigerator (ADR). First, the MKIDs' characteristics were measured without the filters installed to provide a baseline. This involved stepping the temperature of the ADR down from 250mK to 90 mK and recording the MKIDs' responses to a set of frequency sweeps (similar to the one pictured in Figure 2b) conducted at a range of powers. Then, the filters were installed on on the feedline that ran from room temperature to base temperature (see Figure 17), and the same set of measurements was repeated. The code used for these measurement processes is available in Appendix C.

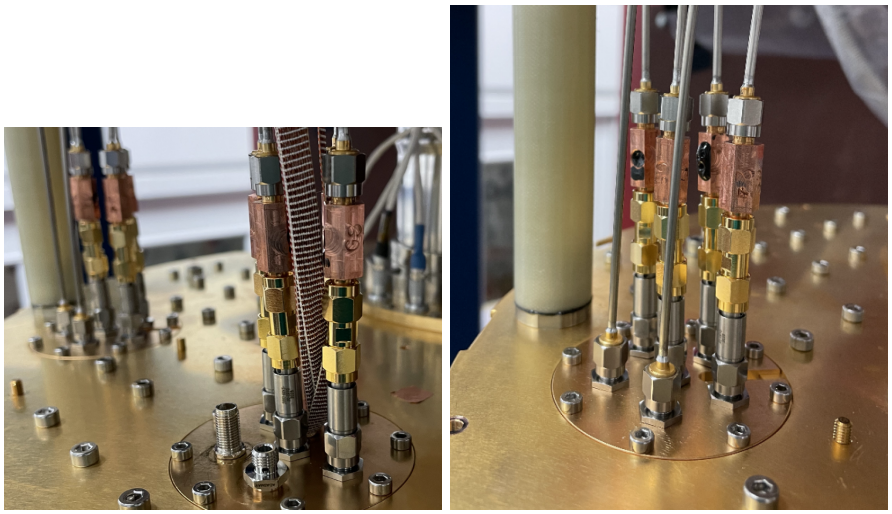

Figure 17: Epoxy filters installed on input lines of the NEXUS dilution refrigerator, in a similar fashion to the installation of filters in the ADR.

The results of the frequency sweeps were fitted to the single-pole resonance behavior approximation (Equation 7) in order to retrieve values for resonant frequency f_r and internal quality factor Q_i for each resonator at each temperature at each input power. The resulting fit results can then themselves be fitted using a well-understood Mattis-Bardeen relation (Appendix D) in order to retrieve the predicted zero-temperature values for the resonant frequency and the internal quality factor, f_0[5] and Q_{i0}. These data points, their fits, and the fit results for two representative feedline powers, of -60 dB and -40 dB are shown in Figure 18 (the related value $df_r/f0$ is shown instead of f_r to facilitate easier comparison between different

[5]The nomenclature becomes slightly confusing at this point; previously f_0 referred to the resonance frequency. Now, f_r is the resonant frequency at some nonzero temperature, and f_0 is the predicted resonance frequency at $T = 0$.

data sets). One dataset taken at Caltech on a different MKID chip that comes from the same silicon wafer and uses the same design as the Al MKID is also plotted for comparison [10]; the power of its feedline signal was roughly equivalent to that of the -55 dB dataset.

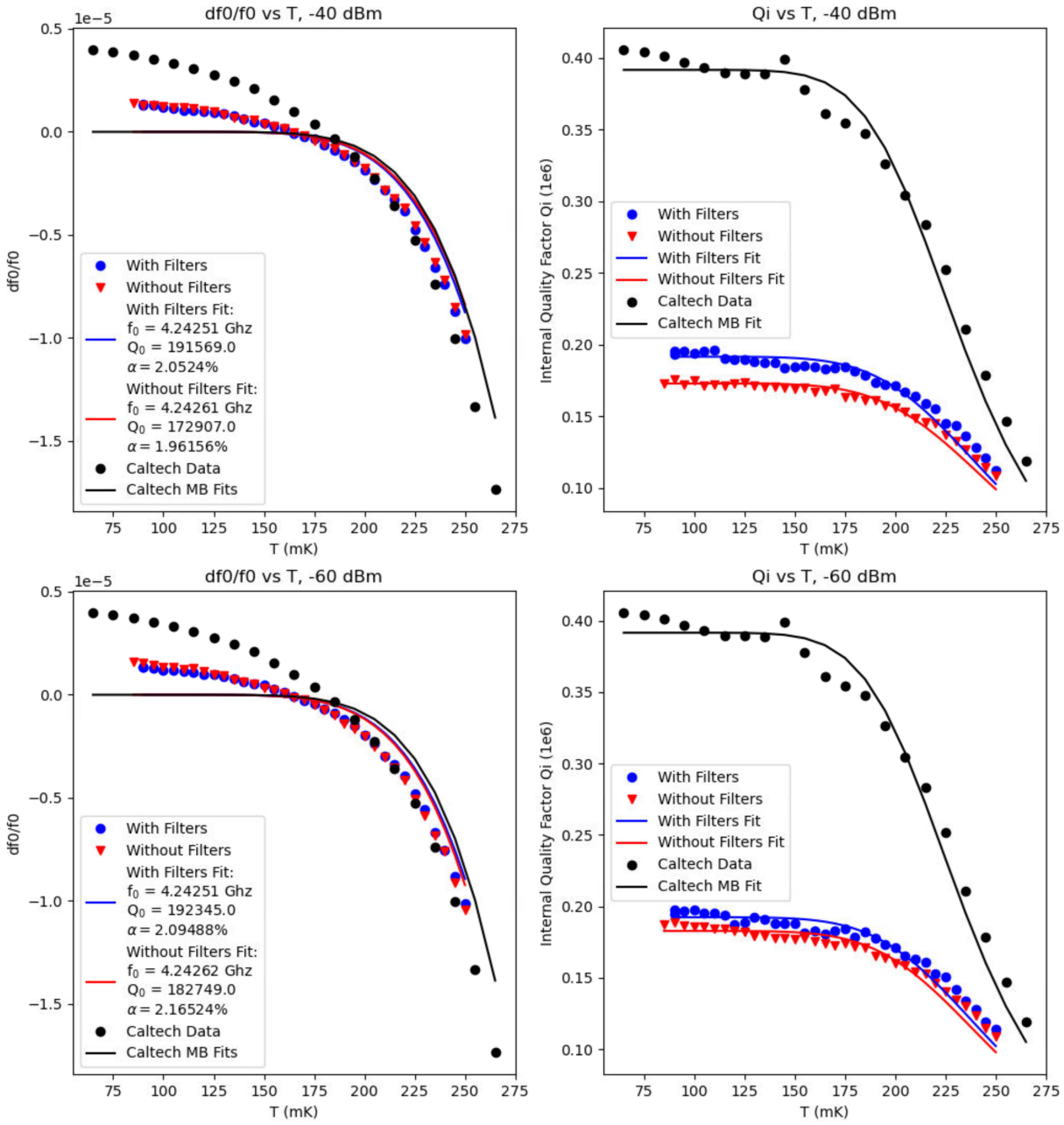

Figure 18: Dependence of fit values for Q_0 and f_r on temperature, measured both with (blue circle) and without (red triangle) the presence of epoxy filters. Data for the same device recorded at Caltech (black circles) is also presented for comparison. Lines represent the predicted curves from the Mattis-Bardeen fits, the numerical results of which are displayed in the legend. Data for feedline powers of -40 dB and -60 dB are shown: all others can be found in Appendix D.

Several details jump out immediately upon inspection. First, the data from Caltech has much higher quality factors across the whole range of temperatures investigated. This effect can easily be explained by the lack of magnetic shielding around the ADR where the second two datasets were recorded. The greater magnetic field present for this data likely resulted in larger amounts of flux becoming trapped during the transitions to the superconducting state. Trapped flux creates normal conducting vortices which can significantly increase the surface resistance of a superconducting film (and significantly decrease its quality factor).

When filters were installed, the Al MKID had consistently higher quality factors at all measured temperatures and feedline powers. The predicted Q_{i0} was also higher for the "With Filters" dataset over the "Without Filters" dataset by an amount that varied depending on feedline power, starting at 3% at -70 dB, rising to 10% at -40 dB, and reaching 42% at -30 dB (Figure 19).The trends for Q_i supports the prediction that the filters reduce the number of incoming IR photons, reducing the number of excess quasiparticles and lowering R_s in accordance with Equation 12. However, f_0 displays the opposite behavior than predicted. The zero-temperature resonant frequencies (from the Mattis-Bardeen fits) with the filters installed were consistently lower than those observed without the filters, and their temperature-dependent offsets from that value (represented by $df_r/f0$) have nearly identical shapes, a trend that opposes that predicted by Equation 11.

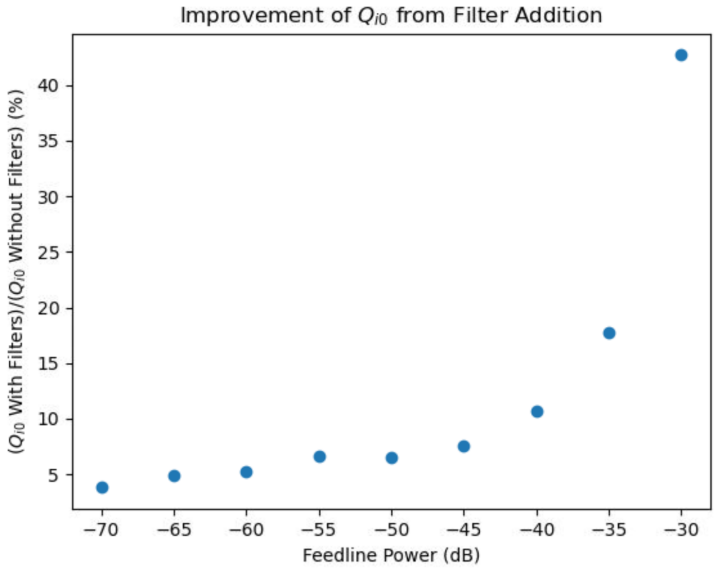

Figure 19: Dependence of filter-driven quality factor increase on feedline power.

The difference in the resonant frequency is most likely the result of the two data sets being taken at different times in different runs of the ADR. This is because the difference between the resonant frequencies is very small compared to the Q_i difference (a factor of $\sim 2.6e-5$ across most powers) but constant across many temperatures, indicating a slight change in the geometric inductance or capacitance of the MKID due

to being temperature-cycled through hundreds of degrees Kelvin. This explanation would account for the temperature invariance of the frequency offset across the small range present in the data sample, because those geometric quantities do not change in response to either temperature or quasiparticle density.

By contrast, the behavior of Q_i in the datasets supports the notion that the difference observed there is a result of true quasiparticle reduction. First, the difference between the quality factors narrows at higher temperatures. This reflects the fact that the thermal quasiparticle population increases with temperature, making the reduction of the population of quasiparticles due to excess pair-breaking less significant. Second, the fractional change in quality factor is orders of magnitude higher than that of the change in resonant frequency. The quality factor is most dependent on the surface resistance, a quantity that has little mechanism for negative change due to temperature cycling (other than a change in the amount of external magnetic shielding, discussed above). Therefore, the increase in quality factor between the filter and non-filter datasets, on average $\sim 12\%$ across all powers, is most plausibly due to the introduction of the filters.

Finally, for Q_{i0} but especially for $df_r/f0$, the Mattis-Bardeen fits diverge from each data set at low temperatures. The most likely explanation for this is a proximity effect occurring between the aluminum film and either the silicon substrate, the adjacent niobium film, or both. This effect would suppress the gap energy below the literature value of 0.17 meV [11] that was kept fixed for the datasets fitted here, thus lowering the temperature scale over which both Q_i and f_r change; this behavior is sometimes termed "gap smearing." The proximity effect happens naturally to varying effects for any thin film, and is exacerbated by high current densities and the near presence of material interfaces. Further investigation is required to determine if the proximity effect is responsible for the divergence from the fits seen in Figure 18, and how it can best be modeled for devices such as MKIDs.

6 Conclusion

The epoxy-based infrared filters described and characterized above were successful in improving the performance of an Al MKID operating in an unshielded ADR, an environment containing high magnetic fields that produced lowered quality factors. Tests are scheduled for the near future involving the same filters and device operating in the NEXUS shielded dilution refrigerator. Results from these tests will hopefully shed light on the impact of these filters in an environment that lends itself to higher resonator quality factors through its lower magnetic field and colder base temperature. Beyond that, many outstanding questions regarding filter and MKID performance remain. These include the source of the performance variance between individual filters, the extent of proximity effects between the MKID's constituent materials, and the efficacy of filters for MKIDs using superconductors other than aluminum. Future investigation along these avenues has the potential to further increase filter performance and MKID sensitivity.

The use of MKIDs for dark matter detection is a relatively young method when compared to many other efforts. As a consequence, many details of their implementation, noise sources and response to events are still being worked out. However, they have massive capacity for multiplexing, a fundamentally athermal nature, and require only room-temperature electronics; all of these characteristics make them attractive phonon detectors for cryogenic dark matter searches looking to scale up their current designs to achieve greater sensitivities.

Whether these favorable characteristics can balance or exceed the relative novelty of MKIDs in the dark matter detection field depends on the effectiveness of experimental techniques to reduce their inherent weaknesses and noise sources. The epoxy-based filters described in this thesis help mitigate one such noise source, infrared photons, but many other noise sources exist and will have to be dealt with.

The technical problems facing MKIDs on an experimental level are very similar in nature to those being faced in the field of superconducting qubits. For instance, the infrared photons that decrease quality factors in superconducting resonators also decrease coherence times in transmons, and the filters described above were heavily inspired by similar filters used to reduce IR noise in quantum computing. It's important that solutions to technical problems in one field continue to be communicated and adapted to analogous problems in others; this filter design is just one example of the importance of collaboration between experimentalists of different fields in order to accelerate the rate of progress in all of them.

References

[1] P. Z. et al. (Particle Data Group), "Review of particle physics 2020," *Prog. Theor. Exp. Phys. 2020*, p. 480, 2020.

[2] B. Cornell, *A Dark Matter Search Using the Final SuperCDMS Soudan Dataset and the Development of a Large-Format, Highly-Multiplexed, Athermal-Phonon-Mediated Particle Detector*. PhD thesis, Caltech, 2018.

[3] J. Zmuidzinas, "Superconducting microresonators: Physics and applications," *Annual Review of Condensed Matter Physics*, 2012.

[4] J. Gao, *The Physics of Superconducting Microresonators*. PhD thesis, Caltech, 2008.

[5] D. C. Moore, *A Search for Low-Mass Dark Matter with the Cryogenic Dark Matter Search and the Development of Highly Multiplexed Phonon-Mediated Particle Detectors*. PhD thesis, Caltech, 2012.

[6] L. Minutolo, B. Steinbach, A. Wandui, and R. O'Brient, "A flexible gpu-accelerated radio-frequency readout for superconducting detectors," *IEEE Transactions on Applied Superconductivity*, vol. 29, p. 1–5, Aug 2019.

[7] K. L. Geerlings, *Improving Coherence of Superconducting Qubits and Resonators*. PhD thesis, Yale, 2013.

[8] Emerson & Cuming Microwave Products, *ECCOSORB MF*, 2008.

[9] M. Fang, "Development of hardware for scaling up superconducting qubits and simulation of quantum chaos," bachelor's thesis, UC Santa Barbara, 2015.

[10] O. Wen, "Unpublished Al MKID dataset." Recorded at Caltech 01/27/20, pre-attenuation output power -35 dB.

[11] C. Kittel, *Introduction to Solid State Physics*. New York: John Wiley & Sons, Inc., 5 ed., 1976.

A Drawings

The original filter enclosure design provided by Robert McDermott's group. Optimal frequency range 1-2 GHz.

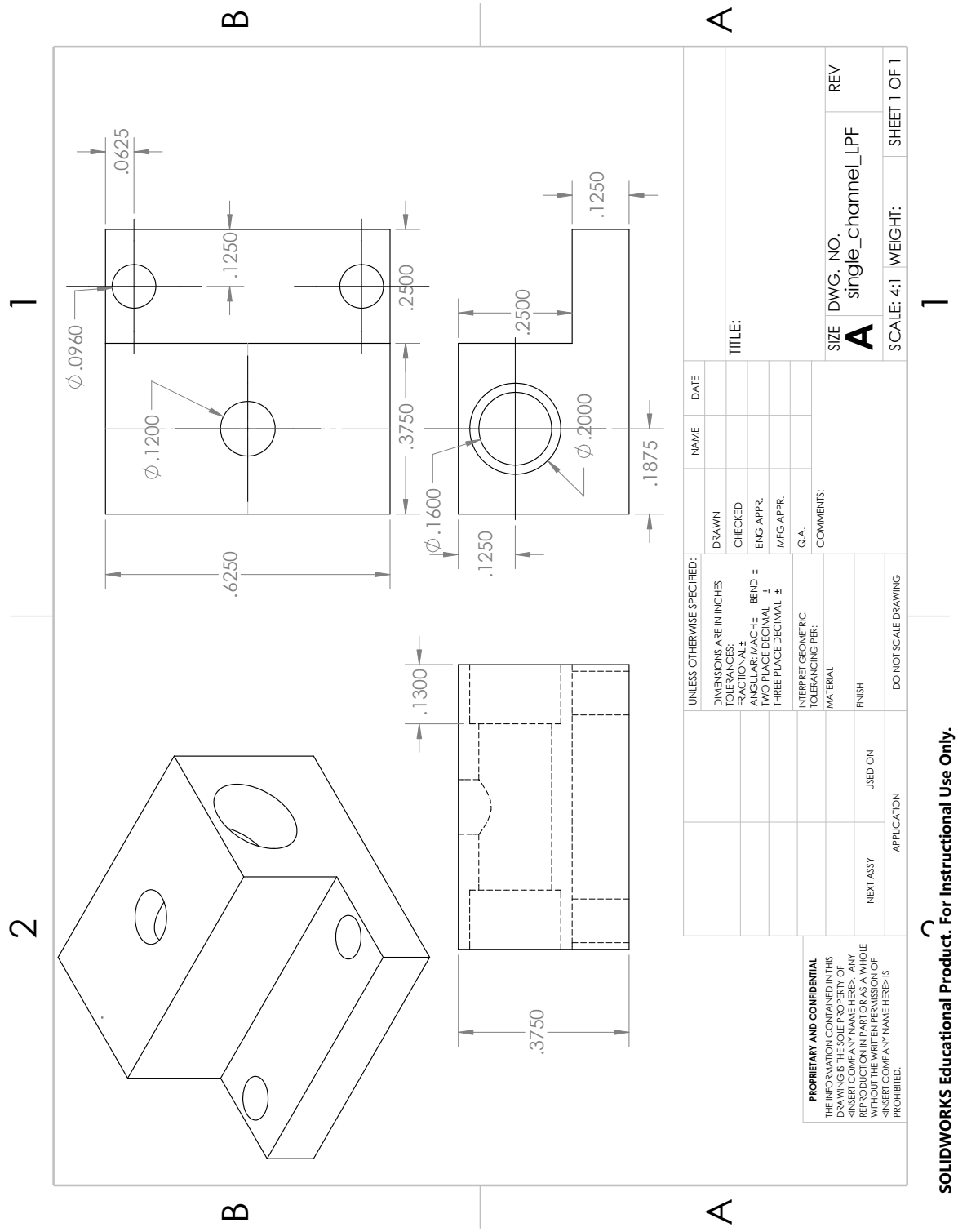

The modified hexagonal filter design produced in this thesis, optimized for 4-8 GHz.

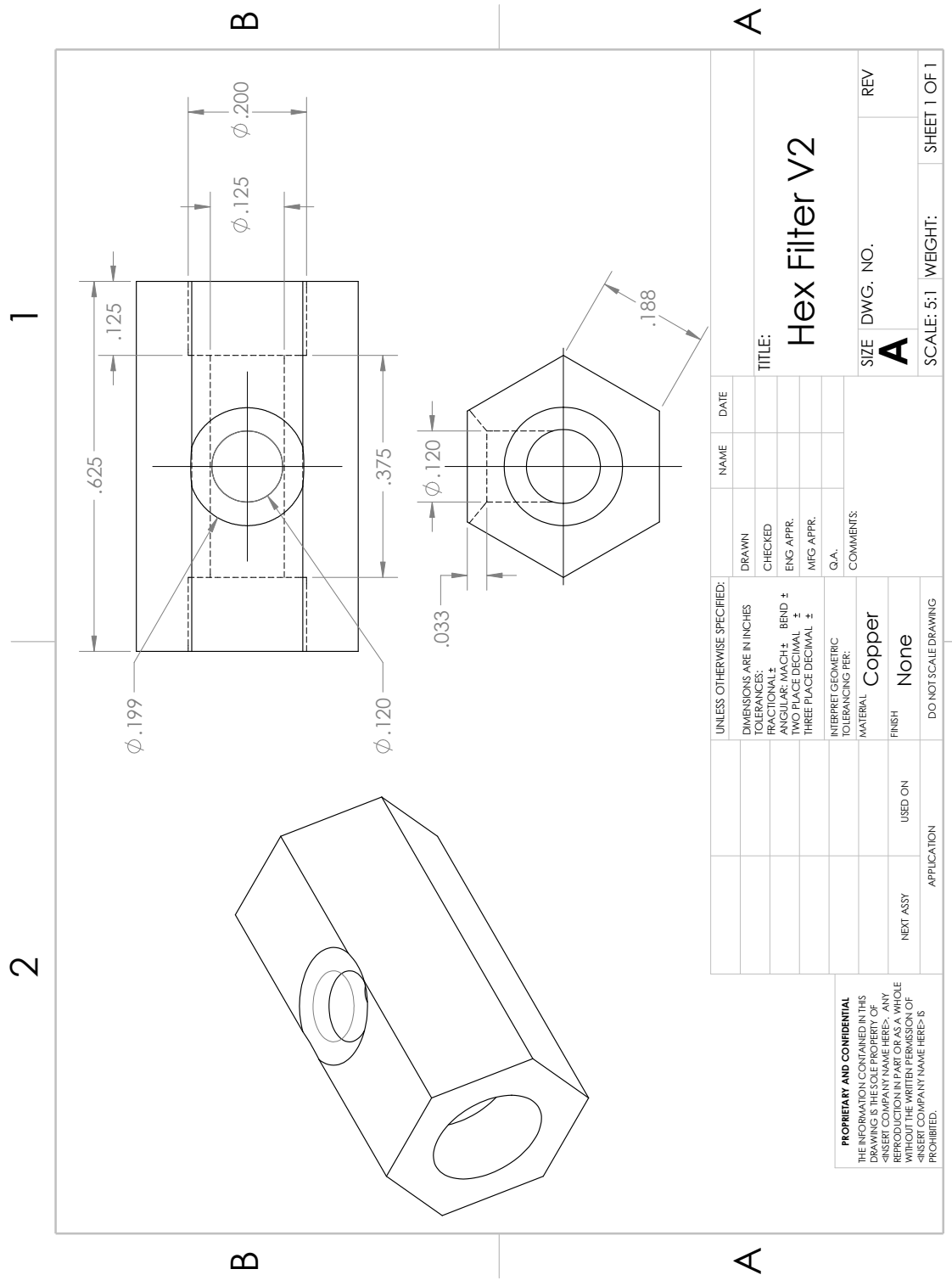

The SMA connector insertion alignment jig, produced as part of this thesis.

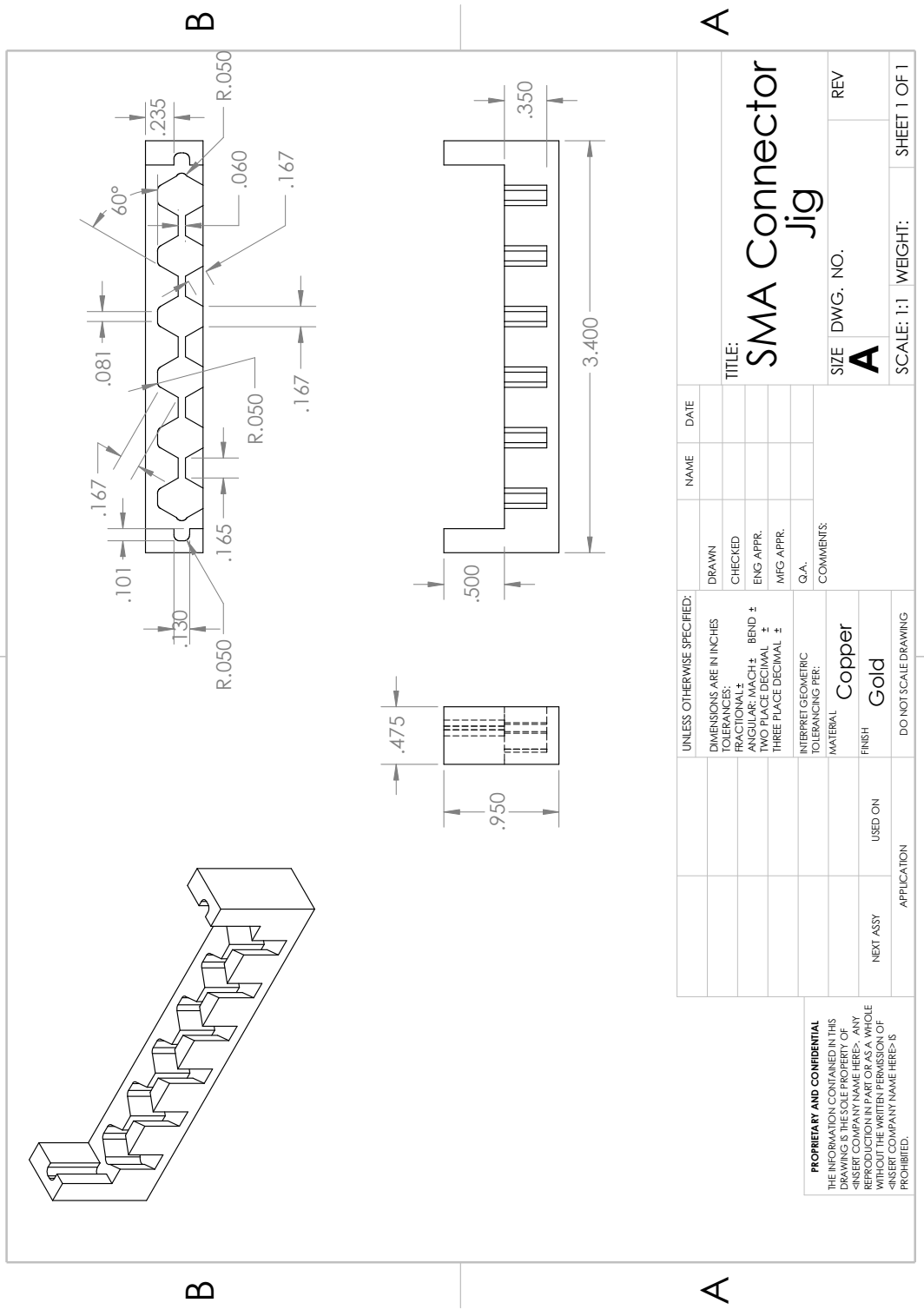

The hex filter body insertion alignment jig, produced as part of this thesis.

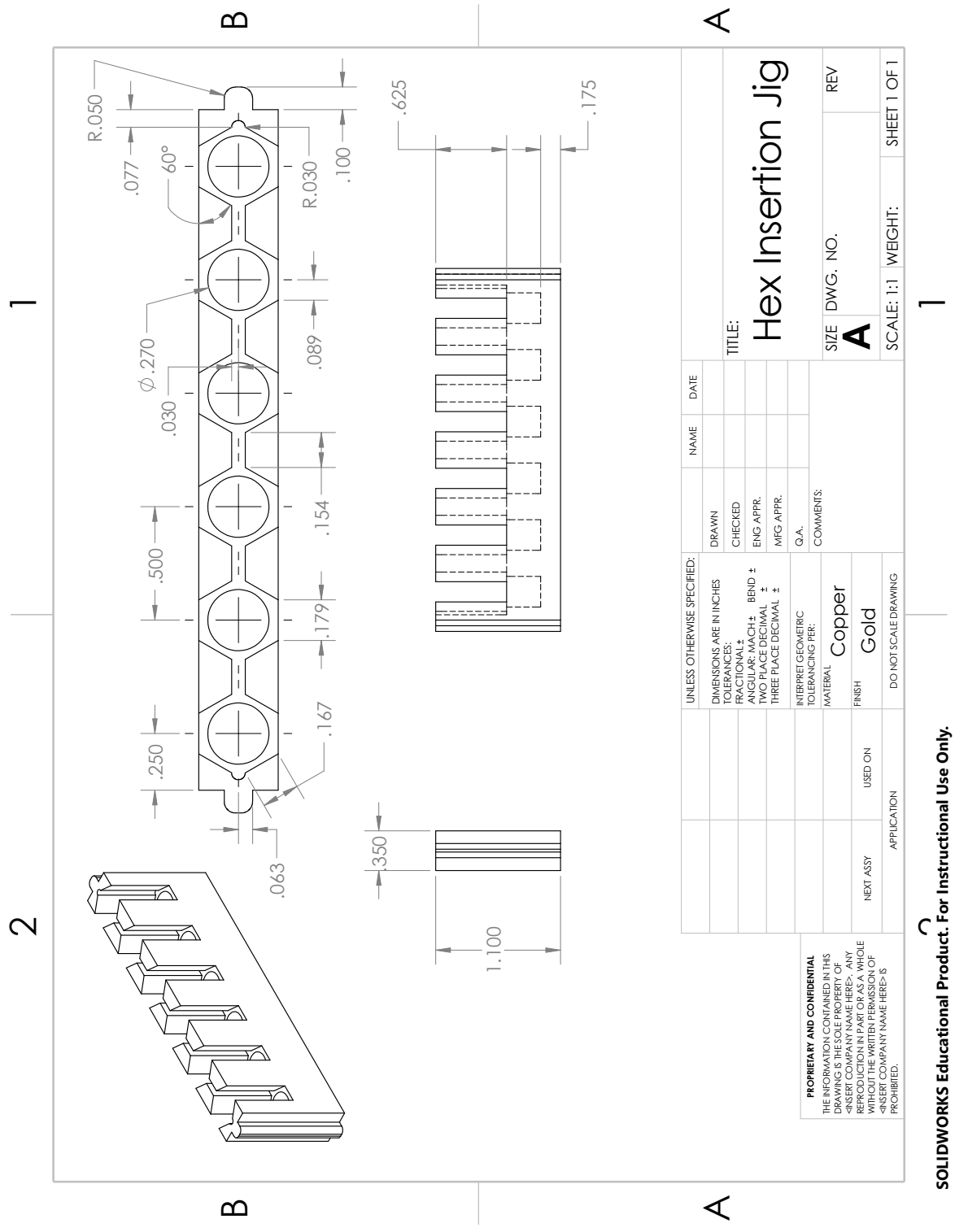

B Filter Performance

The following are VNA characterizations of all successful filters produced in the second production run. Data for filters 04, 08, 13, and 27 are shown in the "Typical Filter Performance" subsection. Data for 28-30 was never taken, as they were reserved for future epoxy mix R&D. For all other numbers 1-30, if the data is missing from the following then the filter did not survive production.

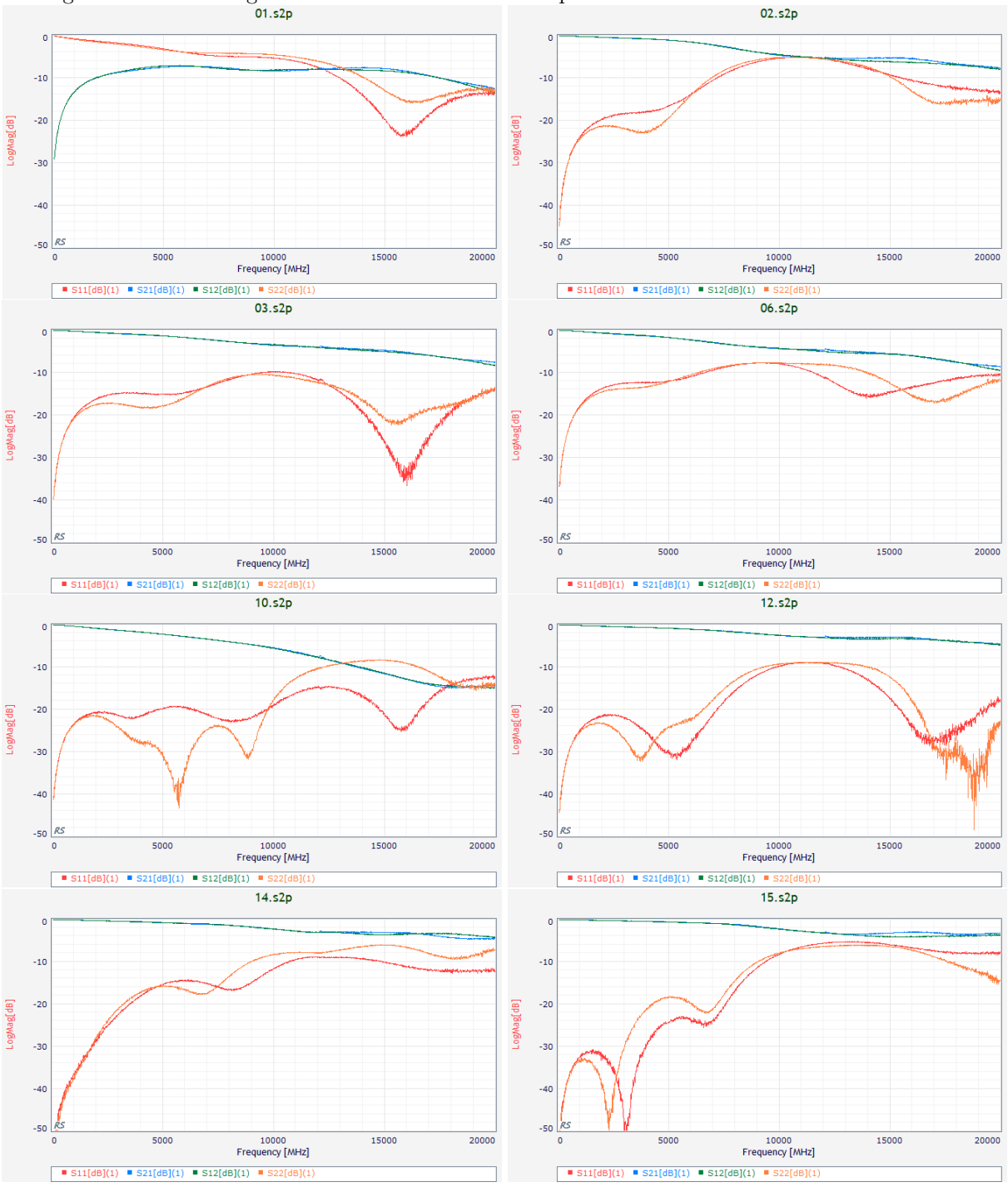

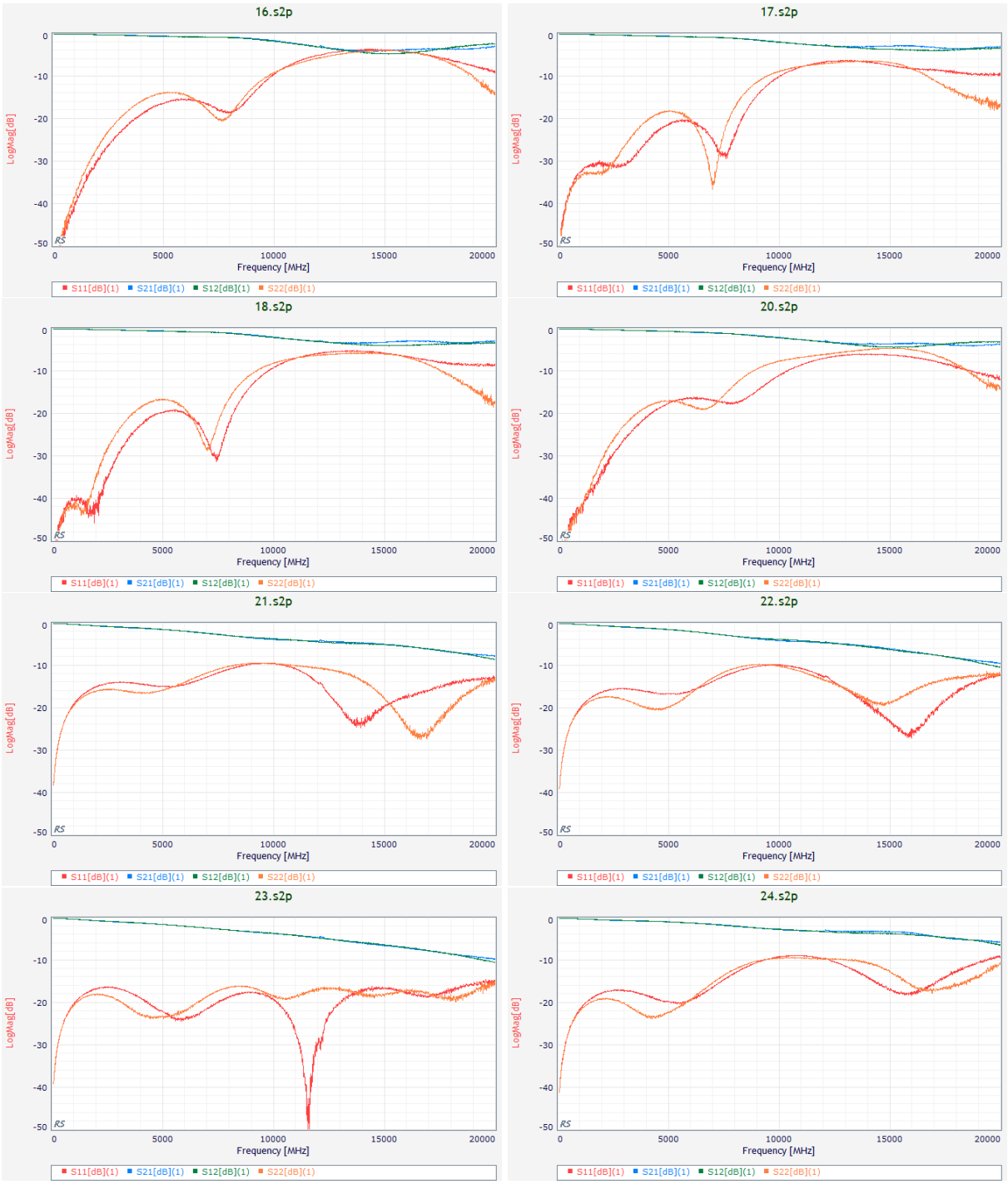
16.s2p
17.s2p
18.s2p
20.s2p
21.s2p
22.s2p
23.s2p
24.s2p
LogMag[dB]
Frequency [MHz]
0
-10
-20
-30
-40
-50
0
5000
10000
15000
20000
RS
S11[dB](1)
S21[dB](1)
S12[dB](1)
S22[dB](1)

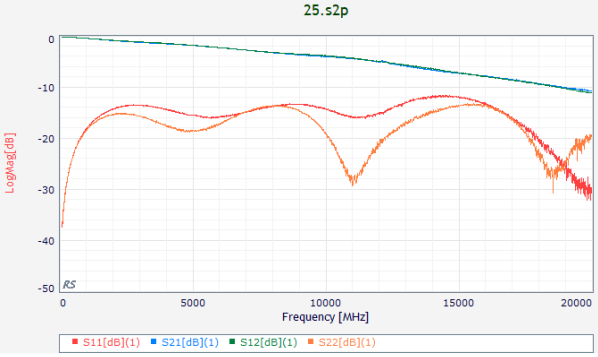
25.s2p
0
-10
-20
-30
-40
-50
LogMag[dB]
RS
0
5000
10000
15000
20000
Frequency [MHz]
S11[dB](1)
S21[dB](1)
S12[dB](1)
S22[dB](1)

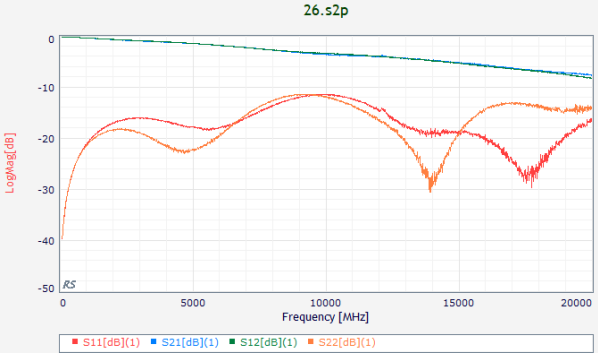
26.s2p
0
-10
-20
-30
-40
-50
LogMag[dB]
RS
0
5000
10000
15000
20000
Frequency [MHz]
S11[dB](1)
S21[dB](1)
S12[dB](1)
S22[dB](1)

C Code

For reading out S_{21} data at a range of temperatures and powers, the following code was written. It assumes an installation of the GPU-SDR server [6] and PyUSRP, a Python library which interfaces with the GPU server. DAQ-specific lines: those that control the temperature of the ADR, those that save the data to a specific output filename.

```
#USRP Script
from __future__ import division
import sys, os
import numpy as np
import datetime
from time import sleep
sys.path.append("../Devices/")

datapath='/data/TempSweeps'
if not os.path.exists(datapath):
    os.makedirs(datapath)

dateStr=str(datetime.datetime.now().strftime('%Y%m%d'))
sweepPath=datapath+'/'+dateStr
if not os.path.exists(sweepPath):
    os.makedirs(sweepPath)

series=str(datetime.datetime.now().strftime('%Y%m%d_%H%M%S'))
print ("Scan stored as series "+series+" in path "+sweepPath)

from ADRfunctionsUSRP import *

def getTempStr(temp):
    if(temp > 0.099):
        return str(temp*1e3)[:3]
    else:
        return str(temp*1e3)[:2]

try:
    import pyUSRP as u
```

```
except ImportError:
    try:
        sys.path.append('/home/nexus-admin/workarea/GPU_SDR')
        import pyUSRP as u
    except ImportError:
        print("Cannot find the pyUSRP package")

sys.path.append('/home/nexus-admin/workarea/PyMKID')
import PyMKID_USRP_functions as puf
import PyMKID_USRP_import_functions as puf2

timeInterval=10
delayTime_min=5 #minutes
minTemp=85
maxTemp=250
tStep=5

debugPowerScan=False

powers = [-70,-65,-60,-55,-50,-45,-40,-35,-30]

delayTime=delayTime_min*60
nSteps=int(delayTime/timeInterval)

fridge=ADR()

temps = np.arange(minTemp,maxTemp+tStep,tStep)
nTemps = len(temps)

print("Temperature Scan")
print("Min:",minTemp,"Max:",maxTemp,"TStep:",tStep)
print("Time per Step:",delayTime_min,"minutes")

for i in range(0,nTemps):
    temp=temps[nTemps-1-i]*1e-3
    print("#Target Temp:",temp)
```

```
cTemp=fridge.getTemp()
print(cTemp,temp)
if(abs(cTemp - temp) > 1e-3):
    if(debugPowerScan == False):
        fridge.setTempSP(temp)
    for i in range(0,nSteps):
        sleep(timeInterval)
        cTemp=fridge.getTemp()
        print("#  ",i,cTemp)
else:
    print("No Ramp Needed")

cTempStr=getTempStr(cTemp)

print("Temp:"+cTempStr+", Starting VNA Scan")

if not u.Connect():
    u.print_error("Cannot find the GPU server!")
    exit()

for power in powers:
    N_power = 10**(((-1*power)-14)/20)
    print(str(round(-14-20*np.log10(N_power),2)) + ' dBm of power')
    print (str(N_power) + ' is the equivalent number of tones needed to
    split the DAQ power into the above amount')

    output_filename = sweepPath+"/TPsweep"+"_T"+cTempStr+"_P"+str(power)+"_"+series

    vna_file, delay = puf2.vna_run(tx_gain=0, \
                                   rx_gain = 25,\
                                   iter=1,\
                                   rate=200e6,
                                   freq=4.24e9,\
                                   front_end='A',\
                                   f0=1e6,f1=6e6,\
```

```
                                        lapse=5,\
                                        points=5e4,\
                                        ntones=N_power,\
                                        delay_duration=0.01,\
                                        delay_over='null',\
                                        output_filename=output_filename)

    u.Disconnect()

print("Done!")
fridge.rampOff()
```

The following code was written as an alternative to the above code. It uses a Copper Mountain Tech M5xxx series VNA to record the results of the frequency sweeps, and doesn't require PyUSRP or the GPU-SDR server. DAQ-specific lines: those that control the temperature of the ADR, those that save the data to a specific output filename.

```
#CMT VNA script
from __future__ import division
import sys, os
import numpy as np
import datetime
from time import sleep
sys.path.append("../Devices/")

datapath='/data/TempSweeps/VNA'
if not os.path.exists(datapath):
    os.makedirs(datapath)

dateStr=str(datetime.datetime.now().strftime('%Y%m%d'))
sweepPath=datapath+'/'+dateStr
if not os.path.exists(sweepPath):
    os.makedirs(sweepPath)

series=str(datetime.datetime.now().strftime('%Y%m%d_%H%M%S'))
print ("Scan stored as series "+series+" in path "+sweepPath)

from ADRfunctionsUSRP import *
from VNAfunctions import *

def getTempStr(temp):
    if(temp > 0.099):
        return str(temp*1e3)[:3]
    else:
        return str(temp*1e3)[:2]

timeInterval=10
delayTime_min=5 #minutes
minTemp=85
```

```
maxTemp=250
tStep=5
n_avs = 10
#wait_secs = 65
#if_bandwidth = 10e3

debugPowerScan=False

powers = [-50,-47.5,-45,-42.5,-40,-37.5,-35,-32.5,-30]

delayTime=delayTime_min*60
nSteps=int(delayTime/timeInterval)

fridge=ADR()
v = VNA()

temps = np.arange(minTemp,maxTemp+tStep,tStep)
nTemps = len(temps)

print("Temperature Scan")
print("Min:",minTemp,"Max:",maxTemp,"TStep:",tStep)
print("Time per Step:",delayTime_min,"minutes")

for i in range(0,nTemps):
    temp=temps[nTemps-1-i]*1e-3
    print("#Target Temp:",temp)

    cTemp=fridge.getTemp()
    print(cTemp,temp)
    if(abs(cTemp - temp) > 1e-3):
        if(debugPowerScan == False):
            fridge.setTempSP(temp)
        for i in range(0,nSteps):
            sleep(timeInterval)
            cTemp=fridge.getTemp()
            print("#  ",i,cTemp)
```

```
    else:
        print("No Ramp Needed")

    cTempStr=getTempStr(cTemp)

    print("Temp:"+cTempStr+", Starting VNA Scan")

    for power in powers:
        print(str(round(power)) + ' dBm of power')

        output_filename = sweepPath+"/TPsweep"+"_T"+cTempStr+"_P"+str(power)+"_"+series

        v.setPower(power)
        freqs, S21_real, S21_imag = v.takeSweep(4241e6, 4246e6, 5e4, n_avs)

        v.storeData(freqs, S21_real, S21_imag, output_filename)

print("Done!")
fridge.rampOff()
```

Finally, the following code defines the VNA class used in the power-temperature scan script above.

```
import socket
import select
from time import sleep
import math

class VNA:

    def __init__(self, server_ip='127.0.0.1', server_port=5025):
        self.server_address = (server_ip, server_port)

    def _sendCmd(self,cmd):
        s = socket.socket(socket.AF_INET, socket.SOCK_STREAM)
        s.connect(self.server_address)
        s.sendall(cmd.encode())
        s.close()
        return

    def _getData(self,cmd):
        s = socket.socket(socket.AF_INET, socket.SOCK_STREAM)
        s.connect(self.server_address)
        #Clear register
        s.sendall("*CLS\n".encode())
        s.sendall(cmd.encode())
        s.settimeout(120)
        try:
            chunks = []
            data = b''.join(chunks)
            while not "\n" in data.decode():
                chunk = s.recv(4096)
                if chunk == b'':
                    raise RuntimeError("socket connection broken")
                chunks.append(chunk)
                data = b''.join(chunks)

        except socket.timeout:
```

```
            s.close()
            raise RuntimeError("No data received from VNA")

        datavals = data.decode()
        datavals = datavals.rstrip("\n")
        return datavals

#    def _waitCmd(self):
#        s = socket.socket(socket.AF_INET, socket.SOCK_STREAM)
#        s.connect(self.server_address)
#        s.sendall("*OPC?\n")
#        opComplete = s.recv(8)
#
#        return

    def setPower(self, power):
        self._sendCmd("SOURce:POWer "+str(power)+"\n")
        print("SOURce:POWer "+str(power))
        #power should be in dBm

    def getPower(self):
        power=0
        power=self._sendCmd("SOURce:POWer?"+"\n")
        print("power is "+str(power)+" dBm")
        return power

    def takeSweep(self, f_min, f_max, n_step, n_avs, waittime=8.5, ifb=10e3):
        #Set sweep params
        self._sendCmd("SENS:FREQ:STAR "+str(f_min)+"\n")
        self._sendCmd("SENS:FREQ:STOP "+str(f_max)+"\n")
        self._sendCmd("SENS:SWE:POIN "+str(n_step)+"\n")
        self._sendCmd("CALC:PAR:DEF S21\n")
        self._sendCmd("CALC:TRAC:FORM POLar\n")
        self._sendCmd("TRIG:SOUR BUS\n")
        self._sendCmd("SENS:BWID "+str(ifb)+"\n")
```

```
        #Set averaging settings
        self._sendCmd("TRIG:AVER ON\n")
        self._sendCmd("SENS:AVER ON\n")
        self._sendCmd("SENS:AVER:COUN "+str(n_avs)+"\n")

        #trigger sweep
        self._sendCmd("TRIG:SING\n")
        sleep(waittime*n_avs)
        #probably should implement an actual *OPC? query here but
        #that appears to be broken on Python 3?
        #self._waitCmd()
        #Autoscale GUI Display
        self._sendCmd("DISP:WIND:TRAC:Y:AUTO\n")

        data = self._getData("CALC:TRAC:DATA:FDAT?\n")
        fs = self._getData("SENS:FREQ:DATA?\n")

        freqs=str(fs)
        S21=str(data)
        #S21_phase=str(phase_data

        freqs = freqs.split(",")
        S21 = S21.split(',')
        S21_real = S21[::2]
        S21_imag = S21[1::2]

        #print(freqs)
        #print(S21)
        return freqs, S21_real, S21_imag

    def storeData(self, freqs, S21_real, S21_imag, filename):
        fullname = filename+'.txt'
        f = open(fullname, "a")

        f.write("freq (Hz), S21 Real, S21 Imag\n")
```

```
    points=len(freqs)

    i=0
    for i in range(points):
        line=freqs[i]+","+S21_real[i]+","+S21_imag[i]+"\n"
        f.write(line)

    f.close()

    return

def readData(self, fname):
    freqs = []
    real = []
    imag = []
    f = open(fname, "r")

    #remove header
    buffer = f.readline()

    line = f.readline()
    while len(line)>2:
        line = line.rstrip("\n")
        data = line.split(",")
        freqs.append(float(data[0])/1e6)
        real.append(float(data[1]))
        imag.append(float(data[2]))
        line = f.readline()

    f.close()
    return freqs, real, imag

def readData_old(self, fname):
    freqs = []
    real = []
    f = open(fname, "r")
```

```
    #remove header
    buffer = f.readline()

    line = f.readline()
    while len(line)>2:
        line = line.rstrip("\n")
        data = line.split(",")
        freqs.append(float(data[0])/1e6)
        real.append(float(data[1]))
        line = f.readline()

    f.close()
    return freqs, real

def comp2mag(self, real, imag):
    mags = []
    angles = []

    for i in len(real):
        mags.append(math.sqrt(float(real[i])**2+float(imag[i])**2))
        angles.append(math.atan(float(imag[i])/float(real[i])))

    return mags, angles
```

D Mattis-Bardeen Fits

The difference between the changes in $Q_i(T)$ and $f_r(T)$ due to quasiparticle increase and the changes due to equivalent temperature change is small enough to be negligible [4]. Then, the behavior of those two quantities as a function of temperature can be found by integrating Equations 11 and 12, and substituting in for the required values of κ and n_{qp}:

$$Q_i(T) = \left(\frac{\alpha}{\pi N_0}\sqrt{\frac{2}{\pi k_B T \Delta_0}}\sinh(x_i) n_{qp}(T) + \frac{1}{Q_{i0}}\right)^{-1} \tag{17}$$

$$f_r(T) = f_0 - \frac{\alpha}{4\Delta_0 N_0}\left(1 + \sqrt{\frac{2\Delta_0}{\pi k_B T}}\exp(x_i) I_0(x_i)\right) n_{qp(T)} f_0 \tag{18}$$

where we have defined

$$x_i = \frac{1}{2}\frac{\hbar\omega}{k_B T} \tag{19}$$

and

$$n_{qp}(T) = 2N_0\sqrt{2\pi k_B T \Delta_0}\exp\left(-\frac{\Delta_0}{k_B T}\right) \tag{20}$$

Here, N_0 is the single-spin density of states (of aluminum in this case), Δ_0 is the gap energy at $T = 0$ and I_0 is the modified Bessel function of first order.

All three initial fit result datasets (Caltech, With filters, Without Filters) were fit to these relations. It was found that the best fit results were achieved by fixing Δ_0 at the literature value for Al of 0.17 meV [11]. The results for the powers -40 dB and -60 dB have been displayed above in the subsection "Effect on MKID Behavior." The results for all other powers measured (-70 dB, -65 dB, -55 dB, -50 dB, -45 dB, -35 dB, -30 dB) are displayed below. Note: the fit results for the Caltech dataset (when Δ_0 was not fixed) were $f_0 = 4.240$ GHz, $Q_{i0} = 405500$, $\Delta_0 = 0.184$ meV and $\alpha = 3.801\%$.

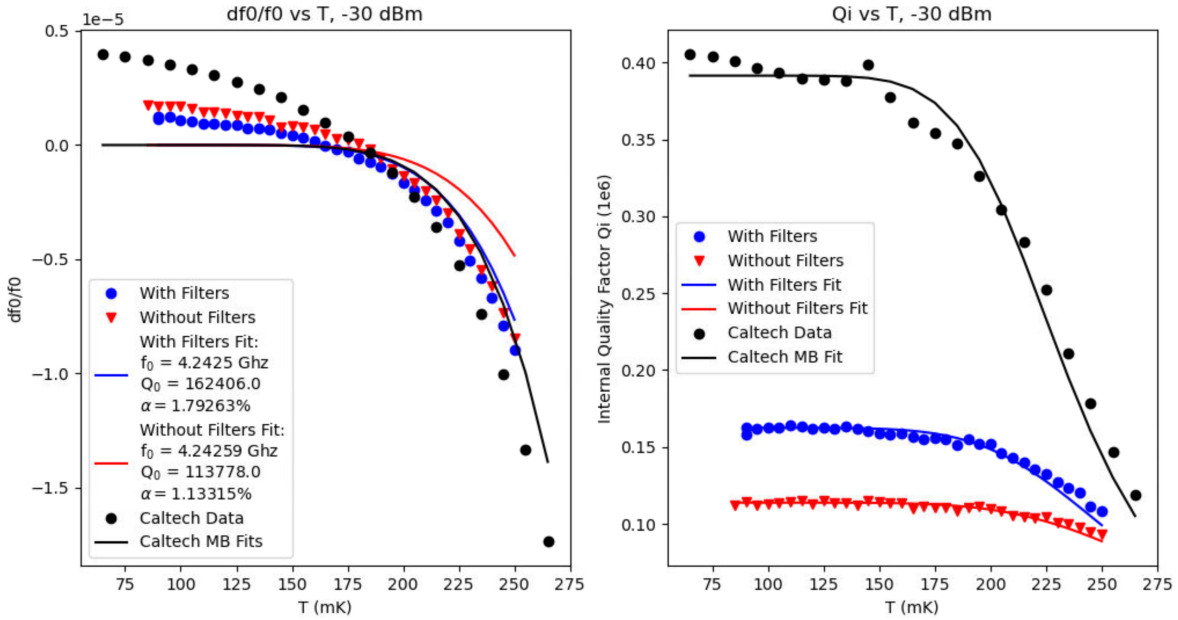

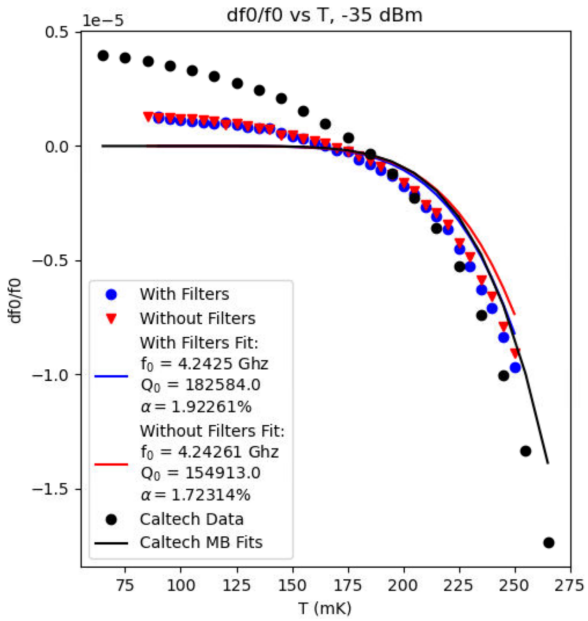
df0/f0 vs T, -35 dBm
1e−5
df0/f0
T (mK)
With Filters
Without Filters
With Filters Fit:
f0 = 4.2425 Ghz
Q0 = 182584.0
α = 1.92261%
Without Filters Fit:
f0 = 4.24261 Ghz
Q0 = 154913.0
α = 1.72314%
Caltech Data
Caltech MB Fits

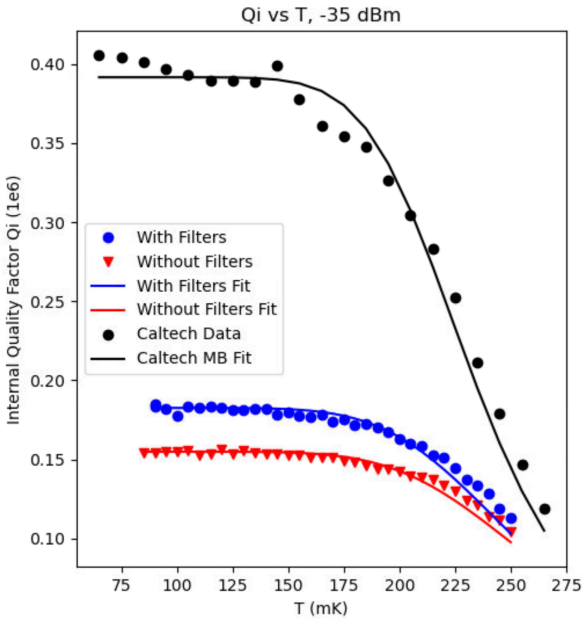
Qi vs T, -35 dBm
Internal Quality Factor Qi (1e6)
T (mK)
With Filters
Without Filters
With Filters Fit
Without Filters Fit
Caltech Data
Caltech MB Fit

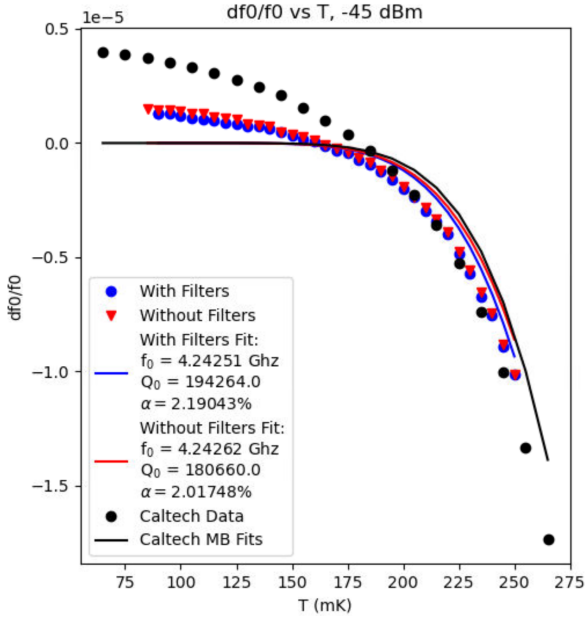
df0/f0 vs T, -45 dBm
1e−5
df0/f0
T (mK)
With Filters
Without Filters
With Filters Fit:
f0 = 4.24251 Ghz
Q0 = 194264.0
α = 2.19043%
Without Filters Fit:
f0 = 4.24262 Ghz
Q0 = 180660.0
α = 2.01748%
Caltech Data
Caltech MB Fits

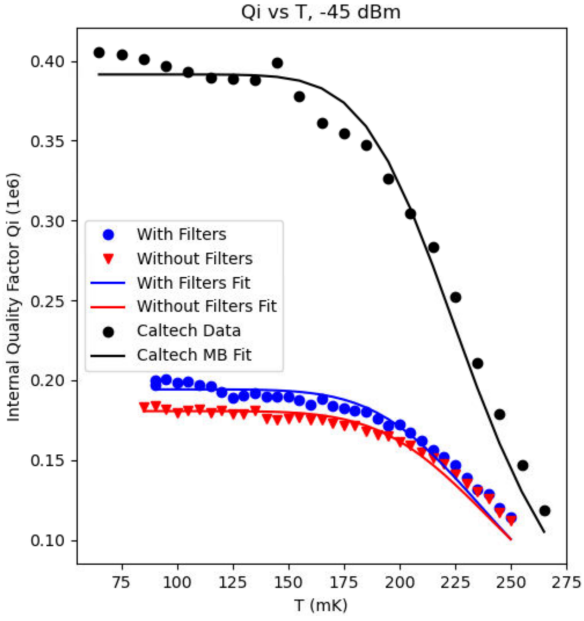
Qi vs T, -45 dBm
Internal Quality Factor Qi (1e6)
T (mK)
With Filters
Without Filters
With Filters Fit
Without Filters Fit
Caltech Data
Caltech MB Fit

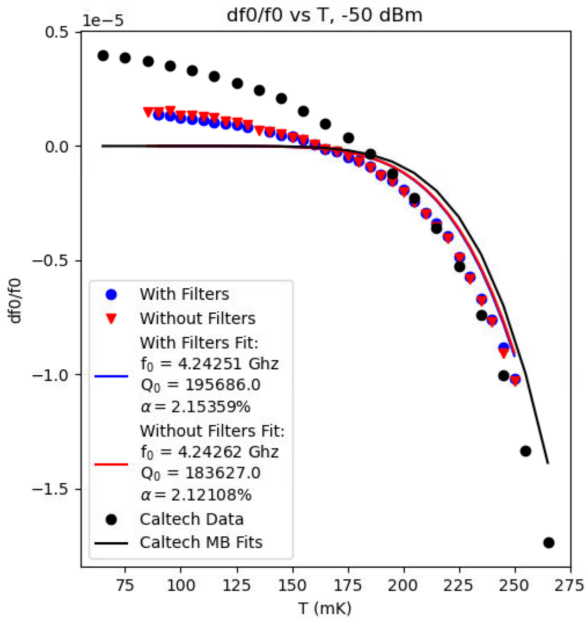
df0/f0 vs T, -50 dBm
1e−5
df0/f0
T (mK)
With Filters
Without Filters
With Filters Fit:
f0 = 4.24251 Ghz
Q0 = 195686.0
α = 2.15359%
Without Filters Fit:
f0 = 4.24262 Ghz
Q0 = 183627.0
α = 2.12108%
Caltech Data
Caltech MB Fits

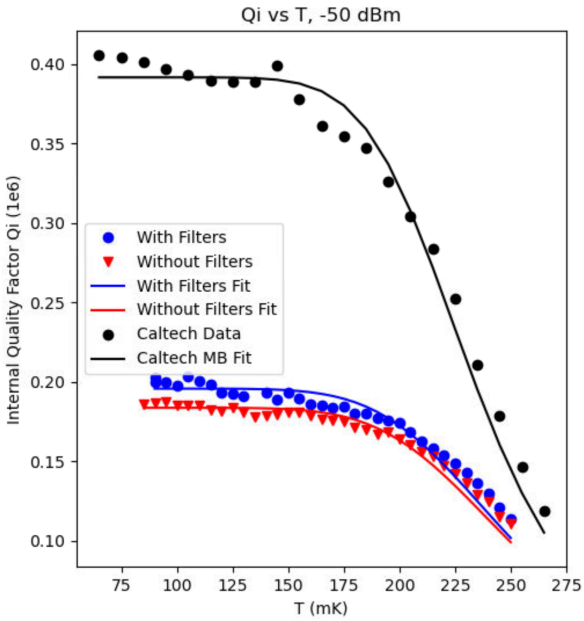
Qi vs T, -50 dBm
Internal Quality Factor Qi (1e6)
T (mK)
With Filters
Without Filters
With Filters Fit
Without Filters Fit
Caltech Data
Caltech MB Fit

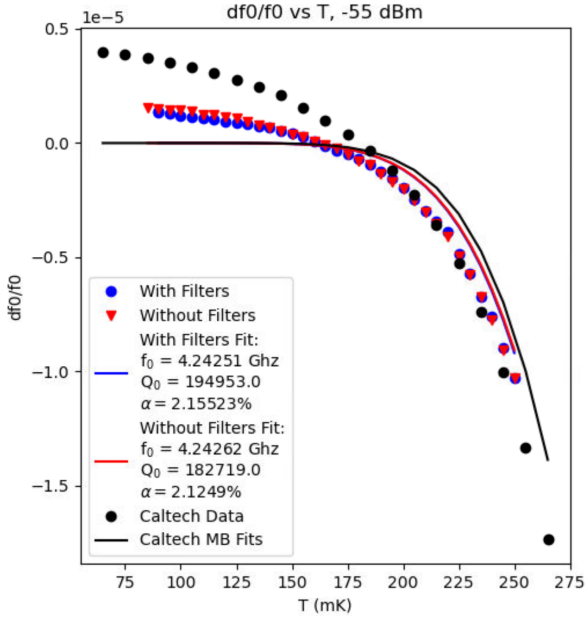
df0/f0 vs T, -55 dBm
1e−5
df0/f0
T (mK)
With Filters
Without Filters
With Filters Fit:
f0 = 4.24251 Ghz
Q0 = 194953.0
α = 2.15523%
Without Filters Fit:
f0 = 4.24262 Ghz
Q0 = 182719.0
α = 2.1249%
Caltech Data
Caltech MB Fits

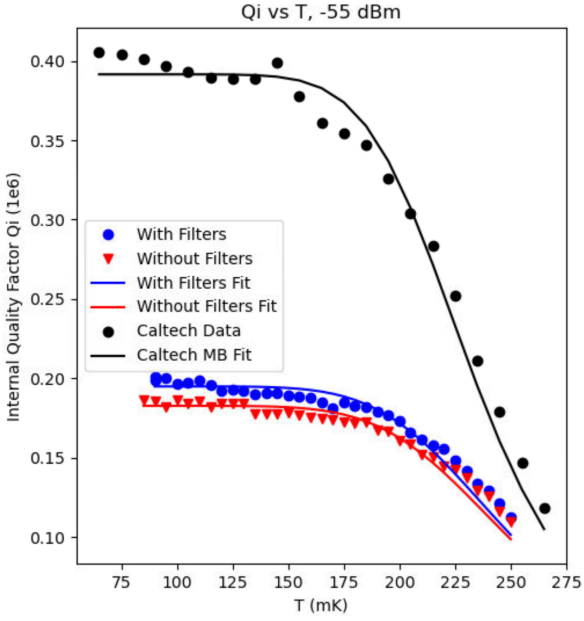
Qi vs T, -55 dBm
Internal Quality Factor Qi (1e6)
T (mK)
With Filters
Without Filters
With Filters Fit
Without Filters Fit
Caltech Data
Caltech MB Fit

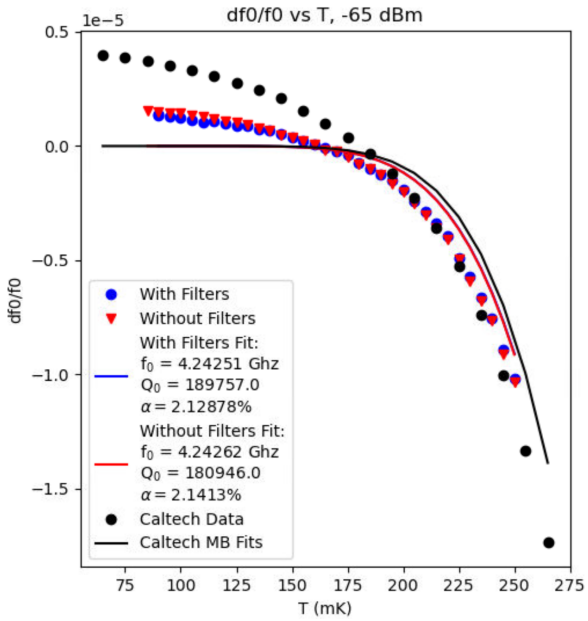
df0/f0 vs T, -65 dBm
1e−5
df0/f0
T (mK)
With Filters
Without Filters
With Filters Fit:
f0 = 4.24251 Ghz
Q0 = 189757.0
α = 2.12878%
Without Filters Fit:
f0 = 4.24262 Ghz
Q0 = 180946.0
α = 2.1413%
Caltech Data
Caltech MB Fits

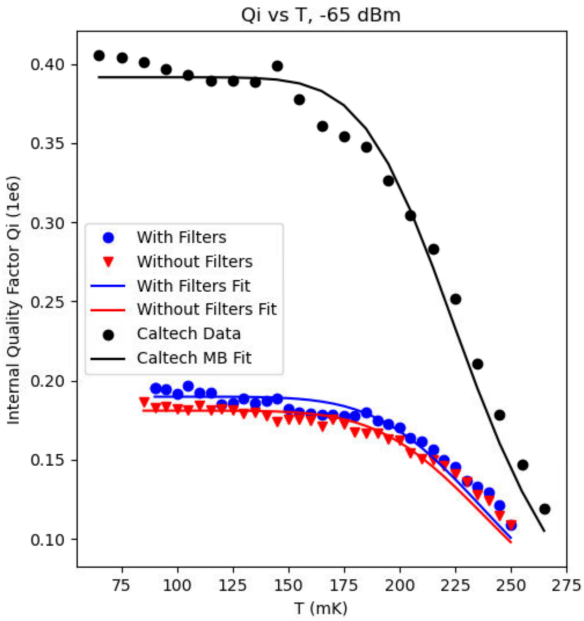
Qi vs T, -65 dBm
Internal Quality Factor Qi (1e6)
T (mK)
With Filters
Without Filters
With Filters Fit
Without Filters Fit
Caltech Data
Caltech MB Fit

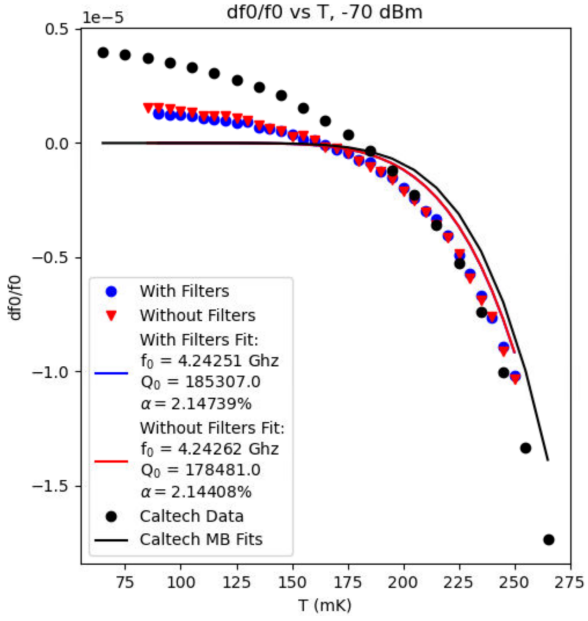
df0/f0 vs T, -70 dBm
1e−5
df0/f0
T (mK)
With Filters
Without Filters
With Filters Fit:
f0 = 4.24251 Ghz
Q0 = 185307.0
α = 2.14739%
Without Filters Fit:
f0 = 4.24262 Ghz
Q0 = 178481.0
α = 2.14408%
Caltech Data
Caltech MB Fits

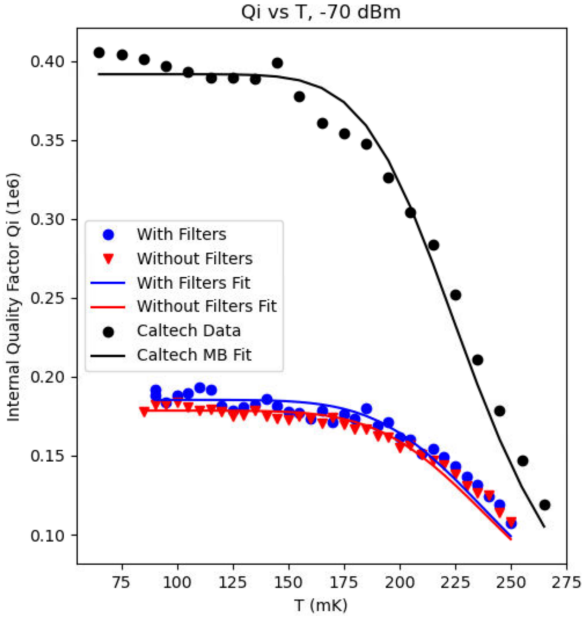
Qi vs T, -70 dBm
Internal Quality Factor Qi (1e6)
T (mK)
With Filters
Without Filters
With Filters Fit
Without Filters Fit
Caltech Data
Caltech MB Fit